International Journal of Digital Earth

ISSN: 1753-8947 (Print) 1753-8955 (Online) Journal homepage: www.tandfonline.com/journals/tjde20

Enabling a Digital Earth for methane emissions management with equal-area discrete global grids

Mingke Erin Li & Steve H.L. Liang

To cite this article: Mingke Erin Li & Steve H.L. Liang (2026) Enabling a Digital Earth for methane emissions management with equal-area discrete global grids, International Journal of Digital Earth, 19:1, 2607210, DOI: 10.1080/17538947.2025.2607210

To link to this article: https://doi.org/10.1080/17538947.2025.2607210

INTERNATIONAL JOURNAL OF DIGITAL EARTH
2026, VOL. 19, NO. 1, 2607210
https://doi.org/10.1080/17538947.2025.2607210

RESEARCH ARTICLE

Enabling a Digital Earth for methane emissions management with equal-area discrete global grids

Mingke Erin Li and Steve H.L. Liang

Department of Geomatics Engineering, Schulich School of Engineering, University of Calgary, 2500 University Drive NW, Calgary, AB, Canada

ABSTRACT

We develop a spatially explicit methane inventory for Alberta's upstream oil and gas sector using the rHEALPix Discrete Global Grid System. The objective is to demonstrate an equal-area, hierarchy-aware framework that assigns facility-reported emissions to native locations and supports multi-scale analysis and reporting. We compile monthly facility activity from Petrinex for 2020 to 2023, geolocate facilities using the Oil and Gas Infrastructure Mapping database, calculate methane emissions from venting, fuel use, and flaring using province-standard factors, and bin results to rHEALPix cells before exact aggregation to coarser levels. Our analysis revealed persistent high-emission hotspots, with 5% of grid cells accounting for 34% of total annual methane emissions. The equal-area lattice enables fair intensity comparisons across latitude, stable hotspot tracking over time, and mass-conserving aggregation that maintains consistent totals across resolutions. Practical implications include a standard spatial fabric that integrates facility reports, satellites, and ground sensors, provides persistent cell buckets for facility and asset management, enables accurate intensity comparisons across space and time with quantitative spatial resolution, preserves spatial integrity in visualization, supports consistent mass conserving aggregation at any scale with multiple granularities for analysis and reporting, allows precise hotspot tracking and trend monitoring, and informs targeted monitoring and survey design.

ARTICLE HISTORY
Received 25 May 2025
Accepted 16 December 2025

KEYWORDS
Discrete global grid systems; rHEALPix; methane emissions; petroleum and natural gas; spatial explicit inventory

1. Introduction

Greenhouse gases (GHGs) are critical drivers of climate change, trapping heat in the atmosphere and altering global climate systems (Masson-Delmotte et al. 2023). While CO_2 is the most prevalent anthropogenic GHG, methane is especially consequential due to its high warming potential (Myhre et al. 2013; Masson-Delmotte et al. 2023). Over 20 years, methane warms nearly 84 times more than CO_2, making its mitigation urgent despite a shorter atmospheric lifetime (Myhre et al. 2013; Masson-Delmotte et al. 2023). In Canada, the oil and gas sector is the largest source of anthropogenic methane emissions, especially in Alberta, British Columbia, and Saskatchewan. According to the Canada Energy Regulator (CER), Alberta alone accounts for 84% of Canada's crude oil and 61% of natural gas production, making it central to mitigation efforts (Canada Energy Regulator 2023). National inventories, including the National Inventory Report (NIR) and the Greenhouse Gas Reporting Programme (GHGRP), provide structured estimates. While national reporting frameworks such as the National Inventory Report (NIR) and the Greenhouse Gas Reporting Programme (GHGRP) provide consistent national and provincial totals and facility-level submissions, many applications, from atmospheric inversion to targeted inspection, require spatially explicit representations that these national totals do not supply.

To meet this need, gridded methane inventories have become foundational inputs for research and policy. Widely used global and continental products, for example, the Emissions Database for Global Atmospheric Research (EDGAR; Crippa et al. 2023), the Global Fuel Exploitation Inventory (GFEI;

CONTACT Mingke Erin Li mingke.li@ucalgary.ca Department of Geomatics Engineering, Schulich School of Engineering, University of Calgary, 2500 University Drive NW, Calgary, AB, Canada

Scarpelli et al. 2020; Scarpelli, Jacob, Grossman, et al. 2022; Scarpelli et al. 2025), the Greenhouse Gas and Air Pollution Interactions and Synergies model (GAINS; Höglund-Isaksson et al. 2020), and the Copernicus Atmosphere Monitoring Service Regional Emissions Inventory (CAMS-REG; Kuenen et al. 2022), provide spatialized emissions that support atmospheric inversions, help interpret observation–model discrepancies, and inform mitigation planning. There are also national and local gridded inventories, for instance, the United States (Maasakkers et al. 2016; Maasakkers et al. 2023), Canada (Scarpelli, Jacob, Moran, et al. 2022), Mexico (Scarpelli et al. 2020), and basin- or state-scale products for California (Jeong and Millstein 2014), the Barnett Shale (Lyon et al. 2015), the Permian Basin (Zhang et al. 2020; Omara et al. 2023), and New York State (Loman and Murray 2025). Section 2.1.1 provides a concise overview of these inventories and their typical use in atmospheric analysis and mitigation planning.

However, two persistent limitations affect their interpretability and reuse. First, most products are distributed on latitude-longitude graticule grids whose cell areas vary with latitude, complicating intensity mapping and scale-consistent aggregation. Second, spatialization typically relies on proxies (e.g. land use or infrastructure density) to allocate activity data, making results sensitive to proxy choice and underlying assumptions. These issues can propagate into downstream modelling and decision support, especially in high-latitude regions and in heterogeneous production basins. We provide a detailed description of these methodological and gridding limitations in Section 2.1.3.

This study demonstrates the application of Discrete Global Grid Systems (DGGS) to construct a spatially explicit methane emission inventory for Alberta’s upstream oil and gas sector, replacing traditional graticule-based grids. DGGS partitions the Earth's surface into equal-area cells, ensuring consistent spatial resolution (Goodchild 2018; Hojati et al. 2022). A key advantage is its ability to eliminate spatial bias, enabling accurate emission analyses and direct inter-cell comparisons (Li and Stefanakis 2020). DGGS also avoids visual deformation of the content, regardless of how the data is presented or the projection used to display it (Li and Stefanakis 2020; Li et al. 2024). Its hierarchical structure allows seamless aggregation across resolutions, supporting multi-scale reporting. This study uses the rearranged Hierarchical Equal Area isoLatitude Pixelization (rHEALPix) DGGS, as detailed in Section 2.2. It also avoids disaggregation methods that may misplace emissions by assigning methane data directly at native resolution, preserving spatial accuracy and minimising allocation errors. The integration of DGGS into GHG monitoring workflows aligns with the vision of a Digital Earth, where global geospatial infrastructures are standardised, scalable, and interoperable. A DGGS-enabled inventory system can facilitate seamless integration of bottom-up emissions data with satellite observations, inversion models, and decision-support tools at global and regional scales.

Despite the centrality of gridded inventories in methane research, there remains a gap in regional, facility-linked inventories built natively on an equal-area, hierarchical grid and demonstrating mass-conserving roll-ups across resolutions. Existing regional products rarely combine all three elements, including equal-area comparability, explicit multi-scale consistency, and direct assignment from facility-reported activity without proxy redistribution. This paper contributes a DGGS-based, equal-area methane inventory for Alberta’s upstream oil and gas sector that (i) assigns facility-reported emissions at native locations to rHEALPix cells; (ii) provides exact, multi-scale aggregation via the hierarchy, preserving mass across resolutions; (iii) quantifies hotspot intensity and persistence using scale-aware summaries; and (iv) enables cross-framework evaluation by converting an existing graticule-based inventory to rHEALPix to diagnose where methodological allocation differences emerge at finer scales. Beyond the case study, we position DGGS as a standardised spatial substrate that can be aggregated exactly to other analysis grids, facilitating integration with inversion systems and decision-support tools.

The remainder of the paper is organised as follows. Section 2 reviews related work on gridded methane inventories and summarises rHEALPix DGGS properties relevant to emissions analysis. Section 3 describes the data and methods, including facility-level calculation, DGGS assignment, aggregation, and visualisation. Section 4 presents the results for Alberta, Section 5 discusses the key findings and implications for methane monitoring and policy applications, and Section 6 concludes the study.

2. Background and related work

2.1 Gridded methane inventories

2.1.1 Overview of existing gridded methane inventories

Extensive efforts have been made to develop gridded methane emission inventories at global, national, and local scales to improve spatially explicit estimates. Several global and continental-scale inventories exist, such as EDGAR, GFEI, GAINS, and CAMS-REG (Höglund-Isaksson et al. 2020; Scarpelli et al. 2020; Kuenen et al. 2022; Scarpelli, Jacob, Grossman, et al. 2022; Crippa et al. 2023; Scarpelli et al. 2025). EDGAR applies IPCC guidelines and spatial proxies, such as land-use and industrial activity data, to allocate national totals to a 0.1 ° × 0.1 ° grid (Crippa et al. 2024). GFEI focuses on fossil fuel exploitation and refines its resolution by incorporating national reports and facility-level production data (Scarpelli et al. 2020; Scarpelli, Jacob, Grossman, et al. 2022; Scarpelli et al. 2025). GAINS provides consistent, policy-oriented emission estimates for all primary greenhouse gases based on integrated energy, agricultural, and waste sector modelling (Höglund-Isaksson et al. 2020). CAMS-REG offers a gridded inventory for Europe, combining reported national totals with updated spatial proxies and sectoral refinements to produce annual emissions at 0.1 ° resolution (Kuenen et al. 2022). At the national scale, inventories have been mainly developed by disaggregating totals using spatial proxies. For the U.S., Maasakkers et al. (2023) produced inventories based on Environmental Protection Agency (EPA) facility data, while Omara et al. (2024) introduced a probabilistic model that integrates empirical measurements to reduce uncertainties. In Canada, Scarpelli, Jacob, Moran, et al. (2022) mapped 2018 NIR methane emissions onto a 0.1° × 0.1° grid, refining oil and gas sector estimates with facility-level data from the GHGRP. Other national-scale gridded inventories exist for Mexico (Scarpelli et al. 2020), Australia (Wang and Bentley 2002), Switzerland (Hiller et al. 2014), and China (Peng et al. 2016; Sheng et al. 2019). Local gridded methane inventories have been developed for New York State, California, the Barnett Shale, and the Permian Basin. For New York State, Loman and Murray, 2025 developed the Gridded New York State inventory at 100 m resolution with monthly time steps across 82 source categories. They reported state totals substantially higher than the U.S. Environmental Protection Agency (EPA) inventory and EDGAR v8, mainly from fossil fuels and landfills. Jeong and Millstein, 2014 created a 0.1 ° inventory for California using EPA factors and activity data, finding oil and gas sector emissions 3 to 7 times higher than official estimates. For the Barnett Shale, a 4 km × 4 km inventory integrated empirical data and Monte Carlo simulations (Lyon et al. 2015). Inventories in the Permian Basin have been updated using improved activity data and emissions characterisation (Zhang et al. 2020; Omara et al. 2023).

2.1.2 Application scenarios of gridded methane inventories

Gridded methane inventories are essential for atmospheric inverse modelling, refining bottom-up estimates by comparing modelled emissions with observations. They provide an initial spatial and sectoral distribution, prevent overfitting, and support interpreting discrepancies between modelled and observed concentrations. Previous studies have demonstrated their importance, with Ishizawa et al. (2024) using a regional inversion to identify discrepancies in western Canada based on EDGAR v4.3.2, Varon et al. (2023) using TROPOMI satellite observations to analyse variability in the Permian Basin with the gridded inventory produced by Maasakkers et al. (2016), and Lu et al. (2022) evaluating methane inventories for North America, incorporating official gridded national inventories for the United States, Canada, and Mexico (Maasakkers et al. 2016; Scarpelli et al. 2020; Scarpelli, Jacob, Moran, et al. 2022). Beyond modelling, spatially explicit inventories support local assessments, enable comparison with top-down measurements, and aid mitigation planning. Top-down measurements include aircraft flux mapping, satellite column retrievals (e.g. TROPOMI and GHGSat), and ground-based mobile or flux-tower observations, which are commonly used to evaluate or constrain bottom-up estimates. Jeong and Millstein, 2014 highlighted their role in validating oil and gas estimates against localised data, while Huang et al. (2024) used them to simulate significant short-term emission events. Given Alberta's vast upstream operations, a region-specific gridded inventory is critical to improving methane monitoring and informing mitigation.

2.1.3 Limitations of existing gridded methane inventories

Most existing gridded inventories rely on graticule-based grids, which introduce several limitations. A major issue is the inconsistent resolution across latitudes, where cell sizes vary due to Earth's curvature. This distorts the visualisation of emission intensity and complicates inter-cell comparisons, especially at higher latitudes. Grids at the equator are roughly equal in area, but those farther north shrink significantly, inflating emission densities in standard projections. Emission intensity per unit area is not straightforward to calculate in graticule-based grids because cell sizes vary. Unlike equal-area grids, where emission intensities are directly comparable across cells, graticule grids require additional calculations to normalise emissions by area. Some gridded inventories report values as emission fluxes, expressing methane intensity per unit area and include the area of each grid cell in their published dataset. For example, Scarpelli, Jacob, Moran, et al. (2022) provide emissions in Mg a^{-1} km^{-2} and give the grid area in m^{-2}. EDGAR inventories distribute both yearly emissions gridmaps (in ton a^{-1}) and emission flux gridmaps (in kg m^{-2} s^{-1}) to support atmospheric modelling applications. While an additional dimension of grid area provides the context, it does not fully resolve the issue, as direct inter-grid comparisons become difficult when moving across latitudes. Additionally, when visualised with standard map projections, size differences can mislead assessments, making emissions appear more concentrated where grid cells are smaller. This can lead to misinterpretation in both qualitative and quantitative analyses, particularly for atmospheric modelling and emissions mitigation.

Moreover, while methodologies vary, most inventories rely on spatial proxies to allocate emissions, and the accuracy of these proxies significantly impacts the final dataset. When used as prior estimates in atmospheric inversion studies, these biases can propagate through the modelling process, potentially leading to discrepancies between modelled and observed methane concentrations. Inventories such as EDGAR have exhibited magnitude errors, with inverse studies requiring substantial upward corrections in the South-Central U.S. (Miller et al. 2013; Wecht et al. 2014; Alexe et al. 2015; Turner et al. 2015). These discrepancies primarily reflect differences in activity data and spatial proxy methodologies, rather than the use of a graticule-based grid. For instance, EDGAR has misallocated oil and gas emissions by assigning them to urban areas instead of production regions, leading to sectoral attribution errors (Maasakkers et al. 2023).

2.2 Rearranged hierarchical equal area isolatitude pixelization (rHEALPix) DGGS

2.2.1 Overview of rHEALPix DGGS

The rHEALPix DGGS is a geospatially adapted variant of the Hierarchical Equal Area isoLatitude Pixelization (HEALPix) system originally developed for the astronomical community. HEALPix, introduced by Gorski et al. (2005), was designed to support cosmic microwave background radiation analysis and is characterised by three key features: hierarchical tessellation, equal-area cells at every resolution, and iso-latitude distribution of cell nuclei along lines of latitude.

Recognising its geospatial potential, researchers at Landcare Research in New Zealand extended HEALPix in 2016 to create rHEALPix DGGS (Gibb 2016). Rather than projecting data onto a celestial sphere, rHEALPix maps data onto Earth's surface, adapting the structure for geospatial analysis (Bowater and Stefanakis 2019b). The system projects a reference ellipsoid (commonly WGS84) onto the faces of a cube, subdivides each face into cells, and then inversely projects the structure back onto the ellipsoid using the rHEALPix equal-area projection (Gibb 2016). This creates a geodesic, specifically a cubic geodesic DGGS, that hierarchically partitions the ellipsoid into equal-area cells across resolutions.

rHEALPix divides the Earth into two zones: an equatorial region (authalic latitudes ≤ 41.8 °) consisting of quadrilateral cells aligned with longitude and latitude (quad cells), and a polar region with variable shapes (Figure 1): (1) Cap cells, centred on the poles and bounded by one parallel; (2) Dart cells, triangular cells with two edges converging at the pole; and (3) Skew quad cells, with edges aligned along parallels (Gibb 2016). The rHEALPix projection combines the Lambert cylindrical equal-area projection for the equatorial region and the Collignon equal-area projection for the poles. As most of Canada lies above 41.8°N, Alberta is primarily composed of skew quad cells.

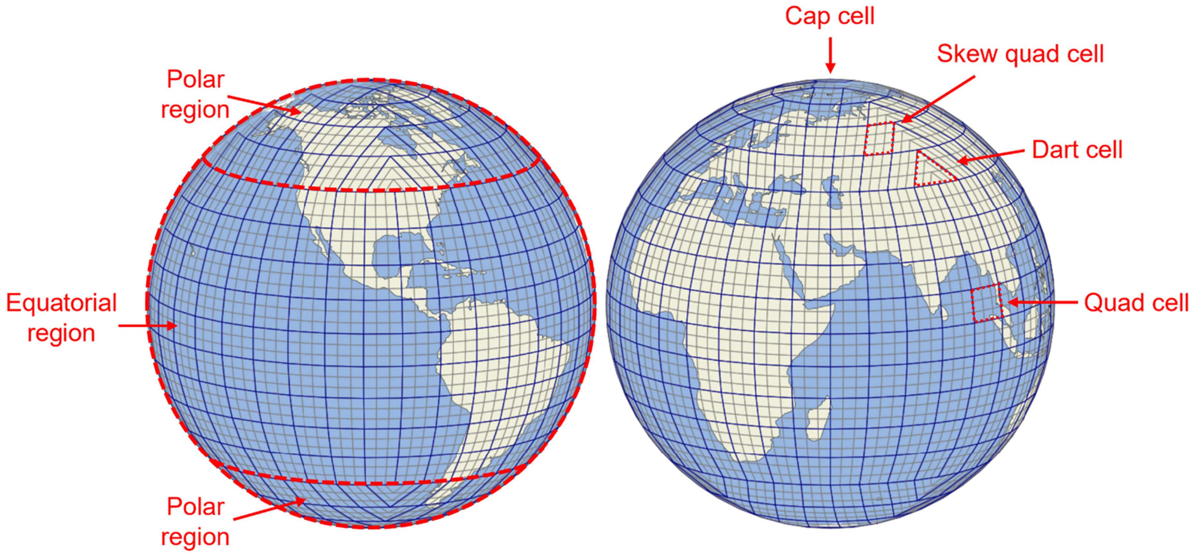

Figure 1. Illustration of cell structures in the polar and equatorial regions of rHEALPix (N_{side} = 3) at resolution levels 2 and 3.

Each cell in the rHEALPix DGGS has a unique identifier. As defined by Gibb (2016), a cell ID begins with one of the letters *N*, S, O, *P*, Q, or R, followed by a sequence of integers (0 to $N_{side}^2 - 1$) assigned using a Z-order space-filling curve from top to bottom and left to right. A general class of DGGSs for any integer $N_{side} \geq 2$ is supported, where each planar cell is divided into $N_{side} \times N_{side}$ child cells at finer resolutions. For this study, the rHEALPix DGGS with $N_{side} = 3$ was used, which means a cell is divided into nine child cells in the next resolution (i.e., refinement ratio equals nine). This choice allows for aligned and congruent hierarchies with the greatest number of resolutions per fixed maximum areal resolution (Gibb 2016). Figure 2 shows the hierarchical cell indexing mechanism in rHEALPix DGGS with $N_{side} = 3$, illustrating how spatial subdivisions occur across resolutions. At resolution 0, the six base cells (*N*, O, *P*, Q, R, S) define the initial framework, which is further subdivided into nine child cells at resolution 1 (Figure 2a,b). Figure 2c demonstrates the continued hierarchical refinement with a detailed example of grid cell “S8” at resolution 2. The centroid of each planar cell serves as the nucleus, and for ellipsoidal cells, the nucleus is defined as the inverse projection of its planar counterpart. Due to the nature of the projection, the nuclei of dart cells and ellipsoidal cells lie on constant-latitude rings (Bowater and Stefanakis 2019a).

Aggregation to coarser resolutions in the rHEALPix DGGS is a straightforward process due to its hierarchical indexing mechanism. As illustrated in Figure 2, descendant cells share a common prefix with their corresponding ancestors, enabling efficient data aggregation without requiring iterative processing across multiple resolutions. Therefore, at any target coarse resolution, methane emissions can be calculated directly by summing the values of all descendant cells from the native resolution. For example, suppose we aim to compute the total methane emissions for the rHEALPix cell with ID “N83” at resolution level 2. In that case, we sum the emissions of all descendant cells from the native resolution whose cell indices begin with “N83”. Since the indexing structure inherently preserves hierarchical relationships, this method eliminates the need for stepwise iteration through intermediate resolutions, making it computationally efficient. It should be noted that aggregation at a coarse resolution level n from precomputed values at a finer, native resolution should yield the same results as direct point binning at resolution n. However, this hierarchical aggregation approach essentially reduces computational overhead by eliminating the need to repeatedly convert geographic coordinates to grid indices, thereby improving efficiency in large-scale methane emission gridded inventories.

The rHEALPix DGGS has been applied in various studies. For example, Bowater and Wachowicz (2020) developed methods to model offset regions around Internet of Things (IoT) device locations, both static and mobile, by quantising them into rHEALPix cells. The Open Geospatial Consortium’s (OGC) Testbed-16 explored DGGS implementations and APIs, identifying rHEALPix as both a reference system provider

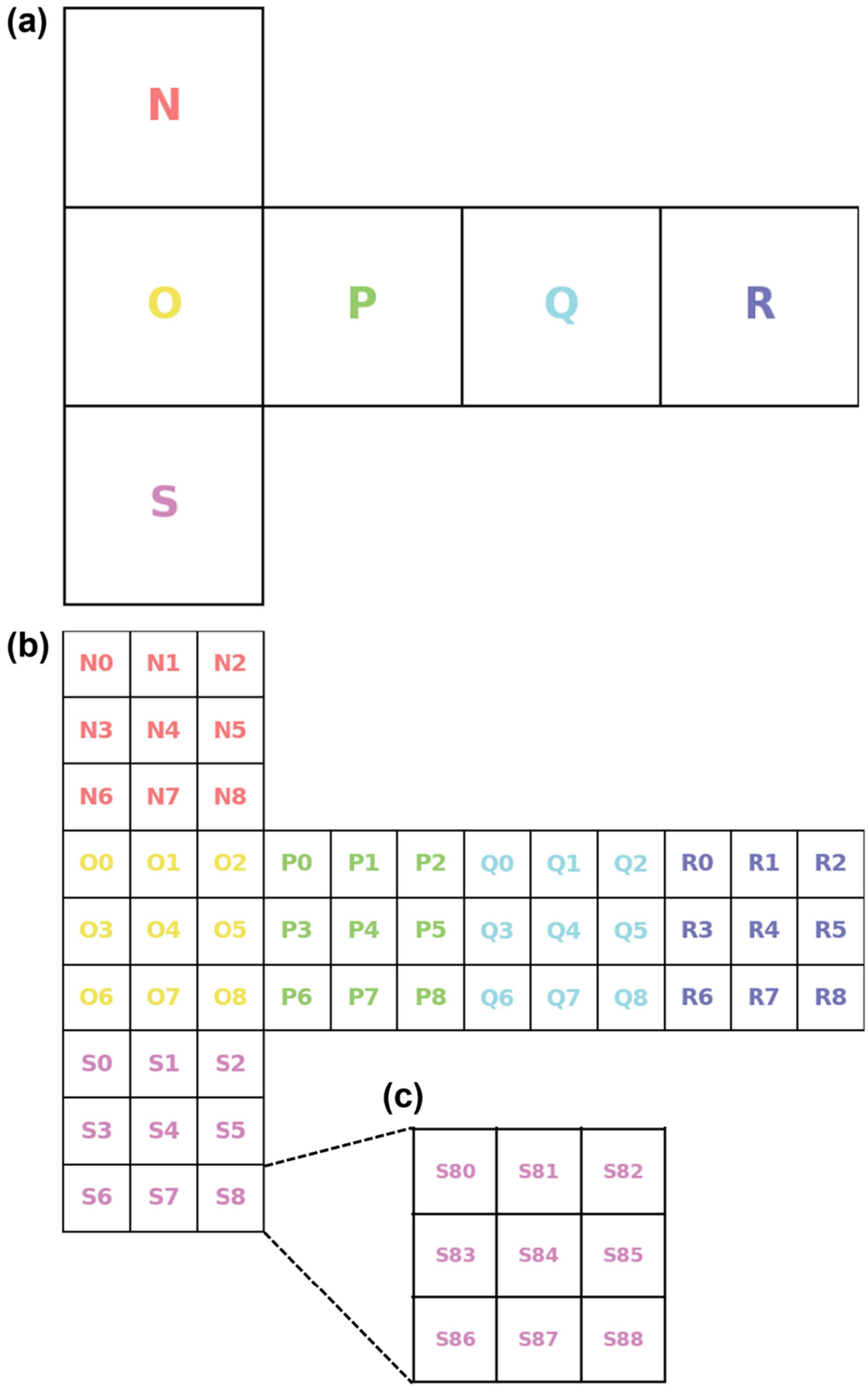

Figure 2. Illustration of rHEALPix cell indexing with $N_{si}d_e = 3$: (a) six base cells at resolution 0; (b) subdivision of each base cell into nine child cells at resolution 1; (c) further subdivision of cell "S8" at resolution 2.

and navigator (Gibb, Cochrane, and Purss 2021). Geoscience Australia adopted rHEALPix in AusPIX, which links points, lines, polygons and rasters to DGGS cells and provides consistent repeatable identifiers (Bell et al. 2020). The rHEALPix is also well-suited to harmonic analysis due to its isohedral cell distribution, with nuclei arranged along constant-latitude rings, an advantage for specific geospatial analyses (Bowater and Stefanakis 2019a). More recently, Gilić and Gašparović (2025) optimised the authalic-latitude conversions used in rHEALPix, reporting approximately 21 times higher numerical accuracy and 2.7 times faster execution for forward transformations, thereby improving equal-area fidelity and runtime in practical implementations.

2.2.2 Properties benefiting methane emission gridded inventories

The rHEALPix DGGS has several properties that make it well-suited for methane emission gridded inventories in Alberta. Its equal-area property, achieved via the Collignon projection in the polar region, ensures each grid cell covers the same surface area, regardless of location. Kmoch et al. (2022) compared various open-source DGGS systems, including Uber H3, Google S2, RiskAware OpenEAGGR, rHEALPix, and DGGRID and found that rHEALPix, OpenEAGGR, and DGGRID's ISEA-based DGGS offered the strongest equal-area guarantees. rHEALPix maintains near-uniform cell areas across latitudes, with variation under 0.01 normalised units (Kmoch et al. 2022). This enables consistent resolution and accurate comparisons between grid cells across regions. Equal-area cells support accurate intensity visualisation and simplify the calculation of emissions per cell. They also eliminate spatial bias caused by variable grid sizes and simplify statistical analysis and regional comparisons.

Another essential feature is the alignment and congruency of cells. For this study, rHEALPix with N_side = 3 was used, producing hierarchical grids with aligned centroids and congruent geometry (Figure 3a). Each parent cell cleanly subdivides into child cells without overlap or gaps, allowing aggregation via simple summation. In contrast, systems like aperture-3 hexagonal tessellations may require additional rules, as child cells can overlap multiple parent cells (Figure 3b). rHEALPix's congruency minimises computational complexity and facilitates cross-resolution analysis.

The rHEALPix DGGS also maintains consistent cell orientation across resolutions. This consistency is due to its tessellation scheme and hierarchical structure, which is based on a cube as the base polyhedron. As a result, the orientation of child cells matches that of their parent cells, ensuring smooth transitions between resolutions during visualisation and improving the interpretability of results. In contrast, some other DGGS alternatives can introduce offsets between successive resolutions, complicating visualisation and analysis. For example, DGGS adopting aperture three hexagonal tessellation has a 30 ° offset between each two consecutive resolutions, as shown in Figure 3.

The hierarchical indexing mechanism employed by rHEALPix DGGS further enhances its suitability for methane emission inventories. Cells within the system are indexed such that their identifiers reflect their hierarchical relationships (Figure 2). For example, a cell with the ID "N8336" is a descendant of cells "N833," "N83," and "N8." This indexing pattern allows for quick aggregation of methane emissions at coarser resolutions by summarising the values of descendant cells at finer resolutions. It avoids the need for time-intensive iterations across resolution levels, as the hierarchical structure inherently organises cell relationships.

Although the system includes a small portion of dart cells in the polar regions, all cells in Alberta are entirely skew quadrilateral cells, which align closely with traditional algorithms for spatial analysis based on square pixels. This alignment simplifies subsequent spatial analyses and computational operations on

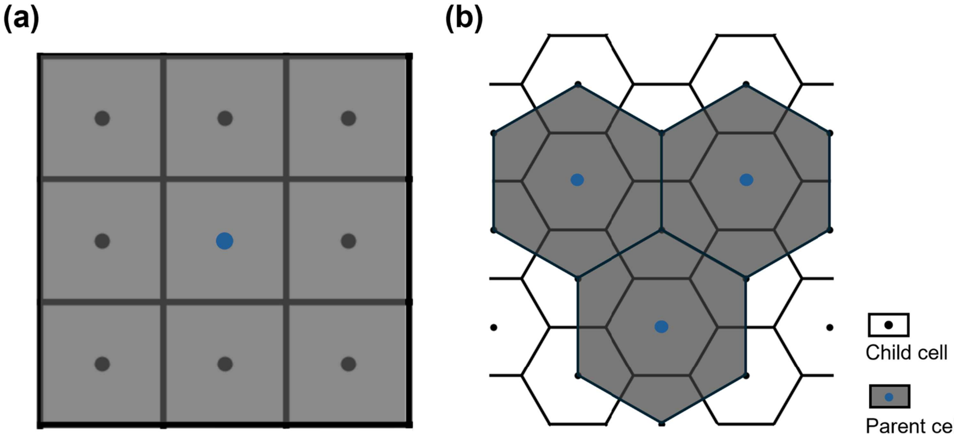

Figure 3. Comparison of parent–child cell construction in two tessellation schemes: (a) aperture-9 square grid, which preserves alignment and congruency between parent and child cells, and (b) aperture-3 hexagonal grid, which introduces rotational offsets and partial overlaps between resolutions.

the methane emission inventory, ensuring compatibility with existing methods and minimising the need for specialised adaptations.

3. Methods

3.1 Data sources

3.1.1 Canada’s petroleum information network (Petrinex)

Petrinex is a centralised, web-based information system that the Canadian petroleum industry uses to streamline and manage the collection, reporting, and exchange of key oil and gas data. It was developed collaboratively by industry stakeholders and governments to enhance operational efficiency, reduce administrative costs, and improve data accuracy. Specifically, Alberta Conventional Volumetric Data, which refers to the reporting and management of production, receipts, dispositions, and other volume-related activities for conventional oil and gas operations, was publicly available via the Petrinex data portal (https://www.petrinex.ca/PD/Pages/APD.aspx) and used in this study. Petrinex serves as a comprehensive and reliable data repository for Alberta's oil and gas industry, as the Alberta Energy Regulator (AER) mandates that each licensee or operator maintain and file monthly activity records under AER Directive 007 (Alberta Energy Regulator 2025). From 2020 to 2023, 25175, 24302, 24272, and 23692 distinct facilities reported their monthly volumetric data through this system, respectively. The Conventional Volumetric Data provides detailed information about reporting facilities, their specific activities, and the products they produce each month. In this study, we focused on the activities of Fuel, Flare, and Vent, which are the primary sources of intended methane emissions from Alberta’s upstream oil and gas sector. The analysis used data from 2020 to 2023, allowing for a multi-year assessment of methane emission trends. According to the updated definitions in the AER Directive 060 (AER 2022), fuel gas refers to the gas combusted to generate energy for upstream operations, while flare gas is combusted in flares or incinerators. Incomplete combustion of fuel or flare gas results in methane and other greenhouse gas emissions into the atmosphere. Vent gas, excluding fugitive emissions, is the uncombusted gas directly released into the atmosphere during upstream operations.

3.1.2 Oil and gas infrastructure mapping (OGIM) database

The OGIM database is a global, spatially explicit dataset of oil and gas infrastructure developed by the Environmental Defence Fund (EDF) and MethaneSAT, LLC (Omara et al. 2023). The OGIM database supports quantification of methane emissions and source characterisation. It complements the Petrinex data by providing detailed geospatial information on oil and gas infrastructure. OGIM v2.5.1, used in this study, contains approximately 6.7 million features globally in the GeoPackage format. The database integrates publicly available geospatial data from government agencies, industry, academia, and other organisations (Omara et al. 2023). For Alberta, data sources include the Alberta Energy Regulator (AER), Petrinex, the Government of Alberta, and Natural Resources Canada (Omara et al. 2023). We focused specifically on Alberta’s facilities, including point feature layers such as oil and natural gas wells, natural gas compressor stations, gathering and processing facilities, tank batteries, petroleum terminals, and injection, disposal, and underground storage facilities. Layers representing offshore platforms, LNG facilities, and crude oil refineries were excluded, as Alberta's oil and gas sector is predominantly onshore upstream. Attributes in these layers include facility ID, type, status, operator, geospatial location, etc. Notably, facility IDs in OGIM align with those in the Petrinex Conventional Volumetric Data, enabling integration of geospatial infrastructure data with activity-based emissions data for this study. While preliminary testing included 2024 Petrinex data, many reporting facilities lacked corresponding spatial records in the 2023 OGIM release. Because accurate geolocation is essential for DGGS assignment, the 2024 data were excluded to maintain spatial consistency. The workflow remains fully extensible and can be readily updated to include additional years once complete spatial records are available.

The integration of Petrinex activity data with the OGIM facility locations established the foundation for quantitative emission estimation. Building on these aligned datasets, methane emissions were then calculated for each facility using activity-specific conversion factors and standardised equations. The datasets described above form the basis for constructing the DGGS-based methane emission layers. The following subsection details how these data were harmonised, standardised, and converted into the rHEALPix DGGS framework.

3.2 Calculation of methane emissions

This step translates reported production and combustion volumes into mass-based methane emissions, providing consistent, facility-level estimates that can later be spatially aggregated within the DGGS framework. Methane emissions from upstream oil and gas operations were calculated based on the activity data reported in the Petrinex system. Different methodologies were applied for Vent, Fuel, and Flare activities to account for the specific mechanisms by which methane is emitted.

For Vent activity, Petrinex reports the total volume of uncombusted hydrocarbon gas released into the atmosphere by each reporting facility. The mass of methane emissions from venting was calculated using the following equation:

$$CH_4^{Vent} = \sum_i (V_i \times f_{CH_4} \times \rho_{CH_4}) \tag{1}$$

where V_i is the total volume of hydrocarbon gas reported by the facility i, f_{CH_4} is the mole fraction of methane in the released hydrocarbon gas, which can be obtained from the Alberta Greenhouse Gas Quantification Methodologies (Government of Alberta 2023). ρ_{CH_4} is the density of methane at standard conditions.

For Fuel and Flare activities, Petrinex reports the total volume of gas combusted at each facility. Incomplete combustion during these processes results in methane emissions. The mass of methane emissions from Fuel and Flare activities was determined using the following equation:

$$CH_4^{Fuel/Flare} = \sum_i (V_i \times EF_{CH_4}) \tag{2}$$

where V_i is the total volume of gas combusted as reported by the facility i, and EF_{CH_4} is the methane emission factor, which represents the mass of methane emitted per unit volume of gas combusted. This factor accounts for the rate of incomplete combustion and differs for Fuel and Flare activities. The appropriate methane emission factors can be referenced from the Alberta Greenhouse Gas Quantification Methodologies (Government of Alberta 2023).

Once facility-level methane emissions were quantified, the next task was to represent them spatially. Using rHEALPix DGGS indexing, each reporting facility was assigned to an equal-area grid cell, allowing emissions to be summed and visualised in a spatially consistent manner.

3.3 Aggregation of point source emissions

To aggregate point source methane emissions, a point-binning operation was applied using the rHEALPix DGGS framework. This process involved mapping individual facility locations to corresponding rHEALPix cells and summing their emissions within each grid cell. First, the geographic coordinates of reporting facilities were converted directly into rHEALPix DGGS cell indices at a predetermined resolution using the rHEALPixDGGS-py library (Raichev, Gibb, and Car 2020). The facility locations were sourced from the OGIM database, which provides spatially explicit infrastructure data for oil and gas operations (Omara et al. 2023). It should be noted that determining the physical footprint of reporting facilities in Alberta is challenging due to the variability in their sizes and configurations. The physical size of these facilities can vary widely based on factors such as production capacity, operational complexity, geographic location, and regulatory requirements. Therefore, there is no single 'correct' resolution for aggregating methane emissions in this scenario, as the choice of native resolution should balance the spatial representation of facilities. The selected resolution should not be much smaller than the typical facility footprint, nor much larger, to avoid excessive fragmentation and over-smoothing. In this study, we chose resolution 9 as the native resolution, with an average cell size of approximately 0.22 km^2, providing a reasonable balance between spatial precision and emission aggregation. The specific characteristics of rHEALPix DGGS across different resolutions, including average ellipsoidal cell width and size, are detailed in Table 1. Once the facilities were assigned to their respective rHEALPix cells, methane emissions were aggregated by summing the calculated values for all facilities within each DGGS cell.

3.4 Aggregation at coarse resolutions

After individual inventories were converted to DGGS cells, multi-scale aggregation was performed to support visualisation and comparative analysis across resolutions. In this study, methane emissions were first converted to the native rHEALPix DGGS resolution corresponding to level 9. Aggregation to coarser levels was then performed using prefix-based cell-ID summation, in which emissions from all descendant cells are summed into their parent cell. This method preserves mass exactly and allows for efficient multi-scale roll-ups without re-projecting or re-rasterising data. The general mathematical formulation and properties of rHEALPix aggregation are described in Section 2.1.

3.5 Conversion of existing graticule-based grids to rHEALPix DGGS

In addition to constructing a DGGS-based inventory from Petrinex data, a comparable conversion was performed for an existing graticule-based methane inventory to facilitate cross-framework evaluation. In this study, we compared the spatial distribution of methane emissions with an existing graticule-based inventory by converting it to the rHEALPix DGGS. A gridded inventory of Canada's anthropogenic methane emissions was developed by Scarpelli, Jacob, Moran, et al. (2022), providing a spatially allocated representation of methane emissions from various source sectors. This gridded inventory distributes methane emissions from Canada's National Inventory Report (NIR) for 2018 onto a $0.1^\circ \times 0.1^\circ$ grid (approximately 10 km × 10 km around the equator), covering the key emission sources such as oil and gas, livestock, solid waste, residential combustion, coal, wastewater treatment and discharge, and other minor contributors. For the oil and gas sector, the study used Petrinex data as one of the activity data sources, specifically for Alberta and Saskatchewan (Scarpelli, Jacob, Moran, et al. 2022). Additionally, facility-level information from Canada's Greenhouse Gas Reporting Programme (GHGRP) was incorporated by retaining the higher value over NIR-based spatially allocated emissions for each grid to enhance grid reliability (Scarpelli, Jacob, Moran, et al. 2022). To maintain consistency with national totals, Scarpelli, Jacob, Moran, et al. (2022) applied a scaling factor to all emissions not derived from the GHGRP, ensuring that the total gridded emissions matched the NIR. The specific magnitude of this scaling factor was not reported in their publication. The resulting dataset is available in netCDF format and is structured to include multiple variables. Each netCDF file contains gridded data representing total sectoral emissions, emissions disaggregated by subsector and source type, the latitude and longitude centres, and the area of each grid cell.

A shared-area principle approach was applied to convert the gridded inventory by Scarpelli, Jacob, Moran, et al. (2022) from netCDF format to the rHEALPix DGGS, ensuring that total methane emissions

Table 1. Summary of rHEALPix DGGS cell dimensions across resolutions.

Resolution level	Average cell width (m, planar)	Average cell area (m^2, ellipsoidal)
0	1.00×10^7	8.51×10^{13}
1	3.34×10^6	9.46×10^{12}
2	1.11×10^6	1.05×10^{12}
3	3.71×10^5	1.17×10^{11}
4	1.24×10^5	1.30×10^{10}
5	4.12×10^4	1.44×10^9
6	1.37×10^4	1.60×10^8
7	4.58×10^3	1.78×10^7
8	1.53×10^3	1.98×10^6
9	509	2.20×10^5
10	170	24408
11	56.5	2712
12	18.8	301
13	6.28	33.5
14	2.09	3.72
15	0.698	0.413

remained consistent before and after conversion. The process began by reconstructing a square-raster grid from the netCDF data, where each data point, defined by a latitude-longitude pair, served as the centre of a raster pixel. The methane emission values from the netCDF file were then assigned to their corresponding raster pixels, each measuring $0.1^\circ \times 0.1^\circ$. Once the raster grid was established, the rHEALPix DGGS grid was overlaid onto it, and each raster pixel could be intersected with multiple rHEALPix cells. The rHEALPix grid grometries were generated using the rHEALPixDGGS-py library (Raichev, Gibb, and Car 2020). The emission value of each raster pixel was proportionally distributed among the overlapping rHEALPix cells based on the shared-area principle, which ensures that the fraction of emissions assigned to each rHEALPix cell corresponds to the proportion of the raster pixel's area that overlaps with that particular cell. For example, in Figure 4, the converted value of the blue rHEALPix grid is calculated using the shared-area principle as follows:

$$r = \sum_i w_i n_i \tag{3}$$

$$w_i = \frac{s_i}{s_{raster}} \tag{4}$$

where n_i represents the original raster pixel value, w_i is the corresponding weight, s_i is the intersected area of the specific raster pixel with the rHEALPix grid cell, and s_{raster} is the original raster pixel area. The raster pixel values are proportionally allocated to the overlapping rHEALPix grid cells based on the area of intersection, ensuring that the total emission value remains consistent across the transformation.

3.6 Visualisation via mapbox globe view

To facilitate the interactive visualisation of the multi-resolution gridded methane inventory, we developed a web-based application using Mapbox (n.d.) to create a globe-centric view. This visualisation framework enables users to explore the spatial distribution of methane emissions at multiple scales while maintaining seamless transitions between resolutions. The visualisation implements scale-dependent visibility, ensuring that coarser-resolution data is displayed at broader spatial extents, while finer-resolution data automatically appears as users zoom in. We provide visualisation for the methane inventory generated in this study

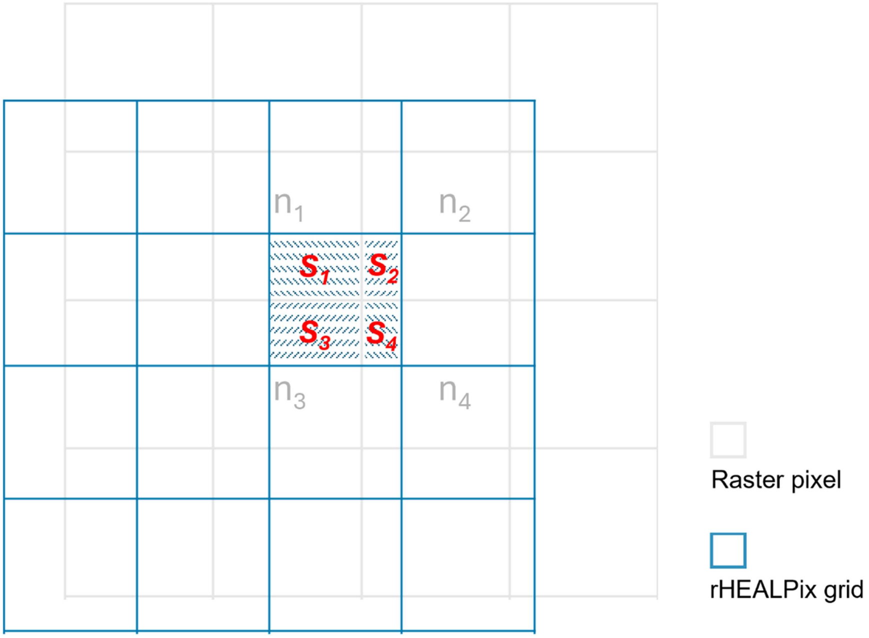

Figure 4. Conversion of raster pixel values to rHEALPix grids using the shared-area principle, where each raster pixel (light grey) is distributed into overlapping rHEALPix grid cells (blue) in proportion to the area of intersection.

and the dataset created by Scarpelli, Jacob, Moran, et al. (2022), which has been converted to the rHEALPix DGGS. The interface includes layer management controls that allow users to switch between datasets within the interface, and an interactive querying feature that enables users to retrieve methane emission values by selecting individual grid cells. For example, Figure 5 illustrates the visualisation of the 2018 gridded methane emission inventory from the oil and gas sector, created by Scarpelli, Jacob, Moran, et al. (2022), and converted to the rHEALPix DGGS. The large-scale spatial distribution of emissions is shown at resolution 5 (Figure 5a), while Figure 5b and Figure 5c demonstrate the interactive querying feature by displaying methane emission values at specific rHEALPix grid cells around Fort McMurray, Alberta. At resolution 5, methane emissions for grid "N83376" are displayed, whereas at resolution 6, emissions are retrieved for the more refined grid "N833761".

It should be noted that the rHEALPix DGGS, like any DGGS with equal-area grid cells, inherently preserves the spatial integrity of the data, regardless of the map projection used for display. This contrasts with traditional projected maps, where different projections can distort the appearance and relative proportions of spatial features, leading to varying interpretations of the same dataset. In the case of a DGGS, although projection may still be required for visualisation, the grid's fundamental structure ensures that cell sizes and shapes remain nearly uniform. As a result, the conveyed information remains consistent

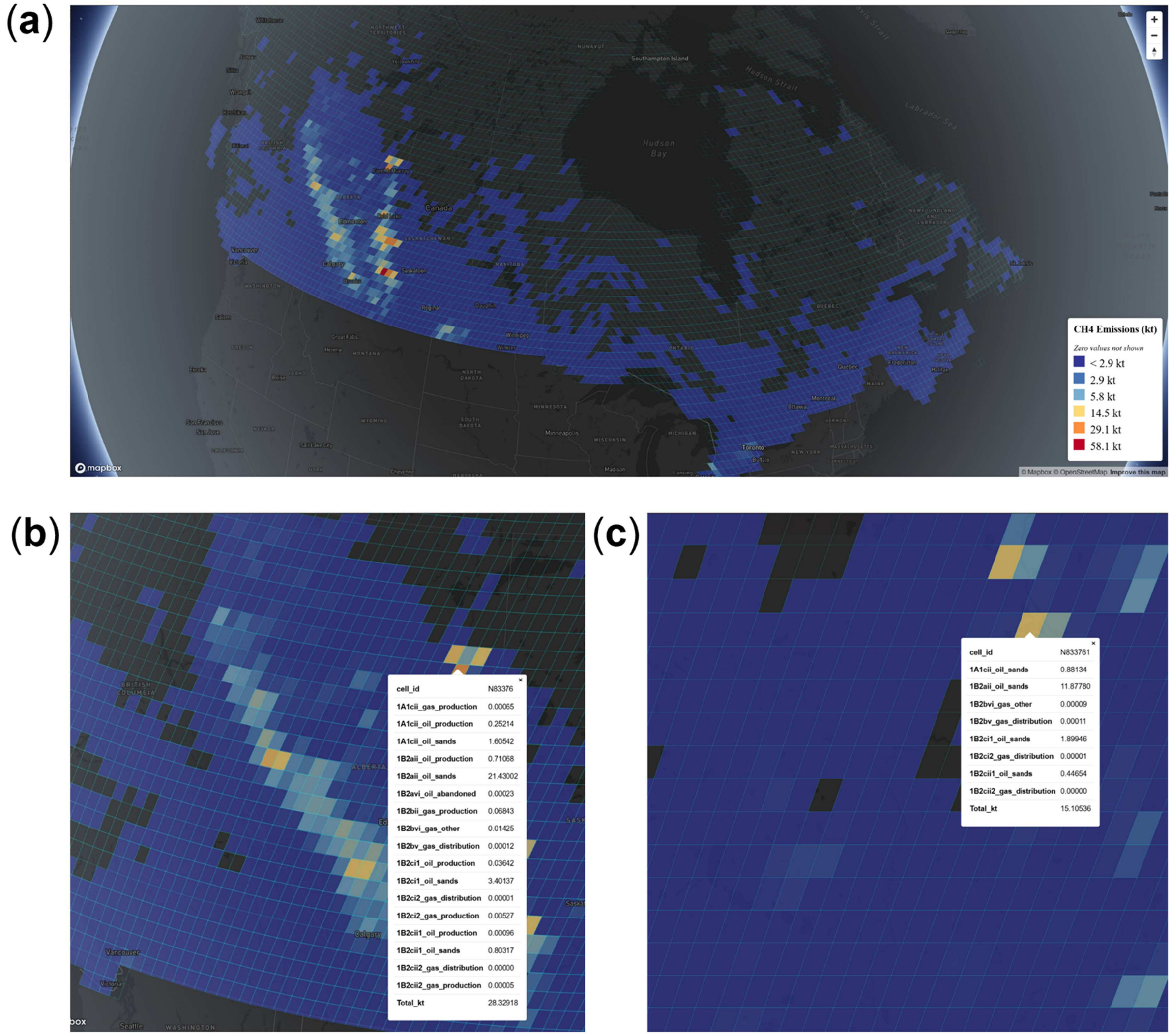

cell_id	N83376
1A1cii_gas_production	0.00065
1A1cii_oil_production	0.25214
1A1cii_oil_sands	1.60542
1B2aii_oil_production	0.71068
1B2aii_oil_sands	21.43002
1B2avi_oil_abandoned	0.00023
1B2bii_gas_production	0.06843
1B2bvi_gas_other	0.01425
1B2bv_gas_distribution	0.00012
1B2ci1_oil_production	0.03642
1B2ci1_oil_sands	3.40137
1B2ci2_gas_distribution	0.00001
1B2ci2_gas_production	0.00527
1B2cii1_oil_production	0.00096
1B2cii1_oil_sands	0.80317
1B2cii2_gas_distribution	0.00000
1B2cii2_gas_production	0.00005
Total_kt	28.32918

cell_id	N833761
1A1cii_oil_sands	0.88134
1B2aii_oil_sands	11.87780
1B2bvi_gas_other	0.00009
1B2bv_gas_distribution	0.00011
1B2ci1_oil_sands	1.89946
1B2ci2_gas_distribution	0.00001
1B2cii1_oil_sands	0.44654
1B2cii2_gas_distribution	0.00000
Total_kt	15.10536

Figure 5. Visualisation of the 2018 oil and gas methane emissions from Scarpelli, Jacob, Moran, et al. (2022), converted to the rHEALPix DGGS. (a) Overview of emissions at resolution 5; (b) grid-level emissions for cell "N83376" near Fort McMurray at resolution 5; (c) resolution 6 view for cell "N833761" at the same location.

and independent of the chosen projection because the cells are known to be almost equal in size and shape (Li and Stefanakis 2020; Li et al. 2024).

4. Results

4.1 Annual methane emissions from Alberta's upstream oil and gas sector (2020-2023)

Methane emissions from upstream oil and gas operations in Alberta varied over the four years from 2020 to 2023 (Table 2). The total methane emissions across all sources, including fuel, flare, and vent, peaked in 2021 at 406.77 Kt a^{-1} and gradually declined to 366.79 Kt a^{-1} in 2023. This decline was primarily driven by reductions in vented methane emissions, which accounted for the largest share of total emissions. Vented methane emissions decreased from 244.49 Kt a^{-1} in 2021 to 201.31 Kt a^{-1} in 2023, with considerable reductions observed in emissions from batteries (BT) and gas gathering systems (GS). However, emissions from flaring increased steadily from 11.48 Kt a^{-1} in 2020 to 16.70 Kt a^{-1} in 2023, primarily due to a rise in reported emissions from batteries (BT). Fuel-related methane emissions remained relatively stable, fluctuating between 144.73 Kt a^{-1} and 149.05 Kt a^{-1} over the four years. In 2020, venting accounted for 59.3% of total emissions, fuel use for 37.8%, and flaring for 2.9%. By 2023, the share of venting had decreased slightly to 54.9%, while fuel emissions remained stable and flaring emissions increased slightly.

When analysing emissions by facility type, batteries (BT) consistently contributed the highest methane emissions, particularly from venting, where emissions exceeded 211.72 Kt a^{-1} in 2020 before declining to 178.00 Kt a^{-1} in 2023 (Table 2). Gas plants (GP) and gas gathering systems (GS) also showed notable contributions across all emission categories. Injection and disposal facilities (IF) exhibited lower emissions across all categories, with fluctuations, particularly in fuel-related emissions, which increased from 28.26 Kt a^{-1} in 2020 to 83.47 Kt a^{-1} in 2023 (Table 2). These trends indicate shifts in operational practices or regulatory changes that may have influenced emission reporting and mitigation measures.

4.2 Spatial distribution and emission hotspots in Alberta

We have identified 12 high-emission hotspot grids at rHEALPix resolution 5 in Alberta, where hotspots are defined as the top 5% of grid cells with the highest methane emissions for each year and persist over the four years from 2020 to 2023. The identified high-emission hotspot grids are primarily located in two regions, the Deep Basin near the Rocky Mountain foothills, which hosts extensive natural gas extraction, and the Athabasca Basin in northeastern Alberta, where large-scale in-situ oil sands operations contribute to persistent methane emissions. Figure 6 illustrates their locations and provides context from two sources: (a) this study's 2020 Petrinex-based emissions at rHEALPix resolution 5, and (b) the Scarpelli, Jacob, Moran, et al. (2022) inventory for 2018, coarsened within the Alberta extent by aggregating the native grid by a factor of three to approximate the cell footprint of Figure 6a without converting to rHEALPix. The

Table 2. Methane emissions from upstream oil and gas operations in Alberta (2020-2023), categorised by Petrinex reporting facility types.

		2020	2021	2022	2023
Fuel (Kt a^{-1})	Total	149.05	148.58	144.73	148.78
	BT	22.31	22.26	22.33	22.41
	IF	28.26	83.58	79.31	83.47
	GP	84.51	28.85	29.37	29.49
	GS	13.98	13.88	13.72	13.42
Flare (Kt a^{-1})	Total	11.48	13.71	14.58	16.70
	BT	7.32	9.04	10.03	11.52
	IF	0.06	0.31	0.04	0.04
	GP	3.18	3.33	3.48	3.78
	GS	0.92	1.03	1.03	1.37
Vent (Kt a^{-1})	Total	233.94	244.49	237.01	201.31
	BT	211.72	219.38	211.75	178.00
	IF	0.48	0.36	0.31	0.38
	GP	8.20	10.59	11.22	9.93
	GS	13.53	14.15	13.73	12.99
Total (Kt a^{-1})		394.47	406.77	396.32	366.79

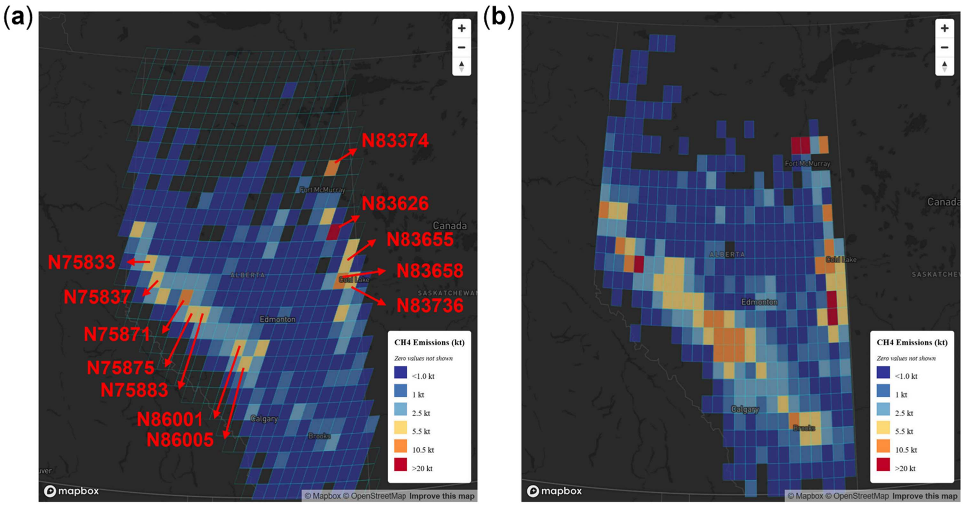

Figure 6. High-emission hotspot grids at rHEALPix resolution 5 in Alberta (i.e. top 5% of cells persisting 2020-2023). (a) This study's 2020 Petrinex-based emissions. (b) Coarse resampled inventory by Scarpelli, Jacob, Moran, et al. (2022) within the Alberta extent, without the conversion to rHEALPix.

Table 3. High-emission hotspot grids at rHEALPix resolution 5 in Alberta, representing the top **5%** of cells with the highest methane emissions persisting from 2020 to 2023. The table summarises facility counts, top-emitting facilities, and annual methane emissions (Kt).

		Highest emitting facility					
Grid ID	Number of facilities	Facility name	Facility type	2020	2021	2022	2023
N75833	147–152	Wapiti S Gas Group 16-36-67-6w6	BT	9.49	11.35	10.69	8.52
N75837	248–262	Gas Effluent Karr 07-11-064-04W6	BT	10.36	11.52	10.69	10.09
N75871	148–166	Petromet Wildriver 10-20	BT	12.38	12.93	12.33	10.08
		Cecilia Wroe 8-12-57-25 MWB	BT				
N75875	66–133	Peyto Oldman 11-17	BT	7.81	7.63	7.69	6.38
		Renaissance Gallaway 12-5	BT				
N75883	140–160	Edson 04-11-053-18W5	GP	7.03	6.63	5.94	4.80
		Edson 1-24-52-20W5	BT				
N83374	4	Firebag Sagd Stage 1 Injection Facility	IF	14.05	15.75	14.76	16.27
N83626	20–26	Cve Christina Lake Leismer 08-17	IF	24.00	25.97	26.00	26.52
N83655	14–16	Primrose East 04-14-067-04W4	IF	10.36	8.51	8.76	8.81
		Primrose North 14-08-068-04W4	IF				
N83658	330–370	Mahikan Injection System	IF	12.79	12.24	16.43	15.96
N83736	117–122	Imperial Mahkeses 15-33	IF	6.12	5.53	5.88	5.58
N86001	477–528	Ferrier -5-45-9W5 Compressor Station	GS	8.20	8.56	8.76	7.90
		Bxe 9-3-44-10W5 Ferrier GS	GS				
N86005	587–594	Willesden Green14-15-039-06 W5M	BT	8.05	8.54	7.42	6.18

coarse spatial correspondence between prominent cells in Figure 6b and our DGGS hotspots in Figure 6a supports the stability of major emitting areas across datasets. Table 3 provides detailed information on the number of facilities within each hotspot grid, the highest emitting facility, and annual methane emissions. The top-emitting facility can be multiple facilities if different across years.

The number of facilities within each hotspot grid varies widely, ranging from as few as four facilities (e.g. grid "N83374") to more than 500 (e.g. grid "N86005"). Despite this variation, all identified grids exhibit persistently high methane emissions. A few large facilities dominate some hotspots, while others contain numerous smaller emitters that collectively contribute to high emissions. In particular, grid "N83374", despite hosting only four facilities, consistently emits over 14 kt per year, indicating a concentration of high-emission activities. Collectively, these hotspot grids emitted 130.63, 135.16, 135.36, and 127.10 Kt in 2020, 2021, 2022, and 2023, respectively, accounting for 33.1%, 33.2%, 34.2%, and 34.7% of total methane emissions. This pattern reveals the spatial concentration of methane emissions, where a small fraction of sites accounts for a disproportionate share of total emissions.

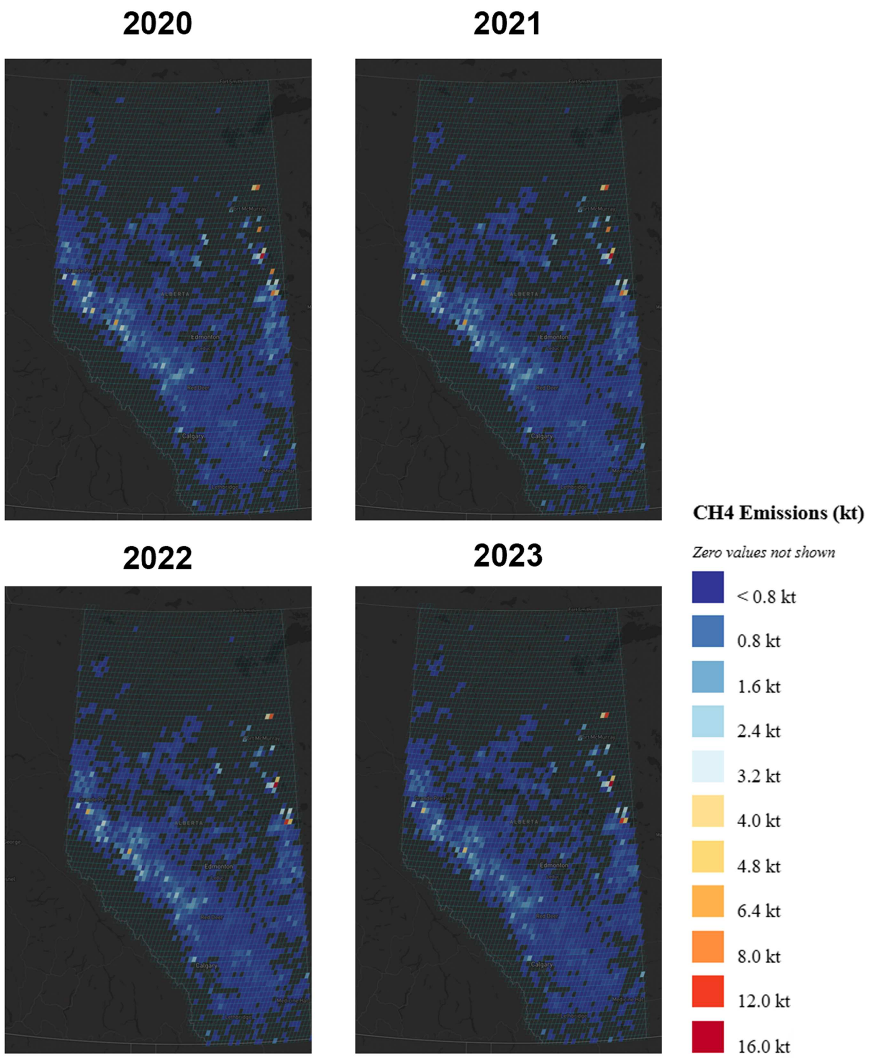

Figure 7. Annual methane emissions from Alberta's upstream oil and gas sector at rHEALPix resolution 6 for years 2020 to 2023, based on Petrinex data.

Figure 7 illustrates the spatial distribution of Alberta's upstream intended methane emissions from 2020 to 2023 at rHEALPix resolution 6, and Figure 8 presents the spatial variations in annual changes. The mean absolute change in methane emissions across all grid cells at resolution 6 was 0.024 Kt in 2021, 0.033 Kt in 2022, and 0.037 Kt in 2023, compared to 2020. Most grid cells showed minimal changes in emissions, suggesting relative stability across much of the region. However, a few individual cells showed large variations due to inconsistencies in facility reporting, where certain facilities reported no emissions in some years but recorded values in others. For example, emissions in grid "N836152" decreased by 7.99 Kt in 2022 and 7.98 Kt in 2023 compared to 2020 (Figure 8). This decline is attributed to two in-situ oil sands facilities operated by ConocoPhillips Canada Resources Corp. (battery and injection sites) that did not report any vent, fuel, or flare activities in 2023. The underlying reason for non-reporting, e.g. inactivity, temporary shutdown, or other reporting circumstances, is outside the scope of this study. Conversely, emissions in grid "N836582" increased by 4.59 Kt in 2022 and 4.41 Kt in 2023, primarily due to the Maskwa Injection System facility, operated by Imperial Oil Resources Limited, which did not report any vent, fuel, or flare activities in 2020 but recorded 3.69 Kt of emissions in 2022 and 3.54 Kt in 2023 (Figure 8).

To analyse the spatial concentration of emissions, we computed the Gini coefficient and Lorenz curve at different resolutions. At resolution 5, the Gini coefficient is 0.73, indicating a moderately uneven

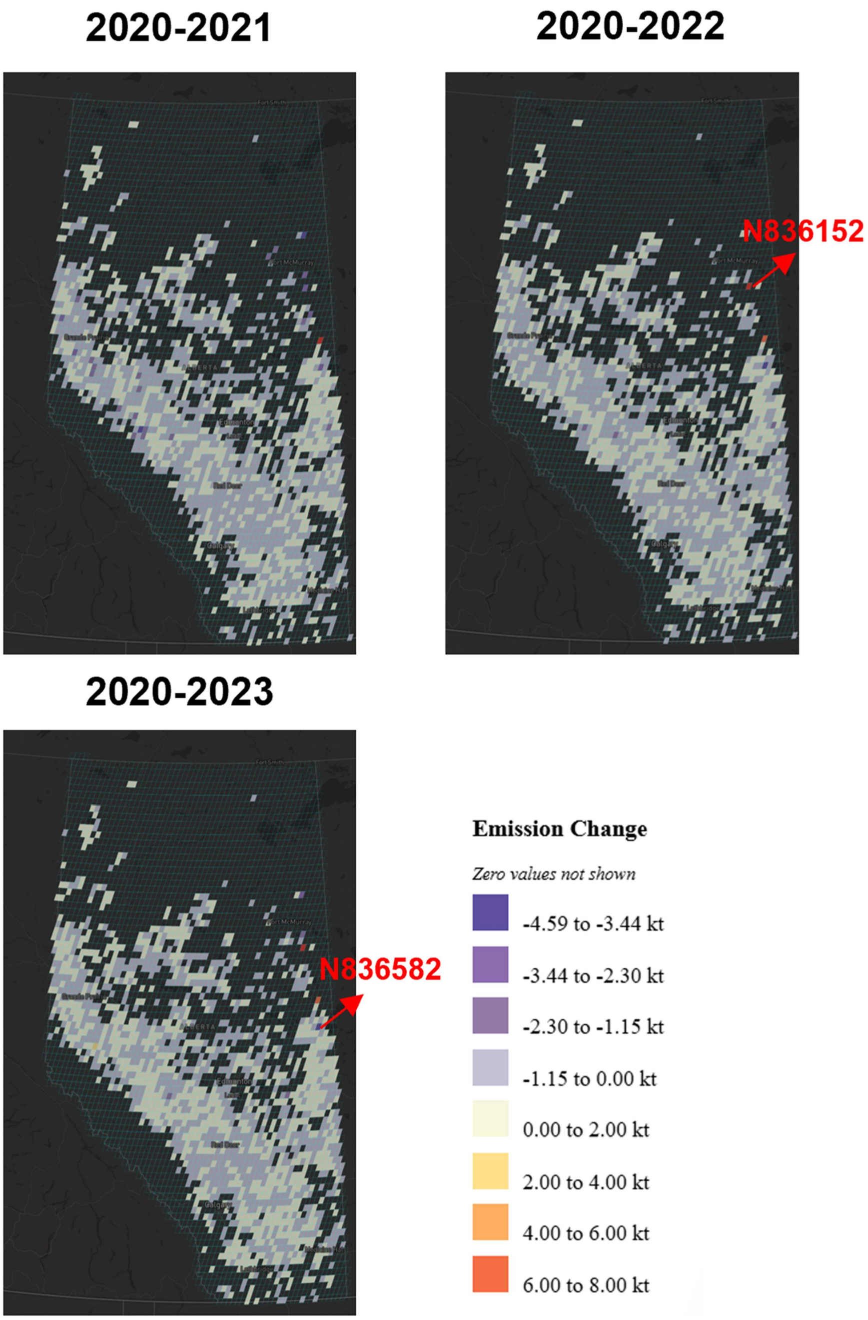
2020-2021

2020-2022

2020-2023

Figure 8. Interannual changes in methane emissions at rHEALPix resolution 6 relative to 2020, based on Petrinex data.

distribution. This value increases to 0.76 at resolution 6, 0.81 at resolution 7, and 0.84 at resolutions 8 and 9, suggesting that emissions become increasingly concentrated within a smaller subset of grid cells at finer spatial scales. The Lorenz curves further illustrate this trend, showing greater deviation from the Perfect Equality line at higher resolutions, reinforcing that a few grid cells account for the majority of emissions (Figure 9).

4.3 Comparison to existing graticule-based gridded inventory

To verify our DGGS conversion process, we compared total emissions before and after conversion against the original Scarpelli, Jacob, Moran, et al. (2022) gridded inventory. The absolute difference between the two totals was approximately 0.2%, confirming that mass was effectively conserved during conversion. To

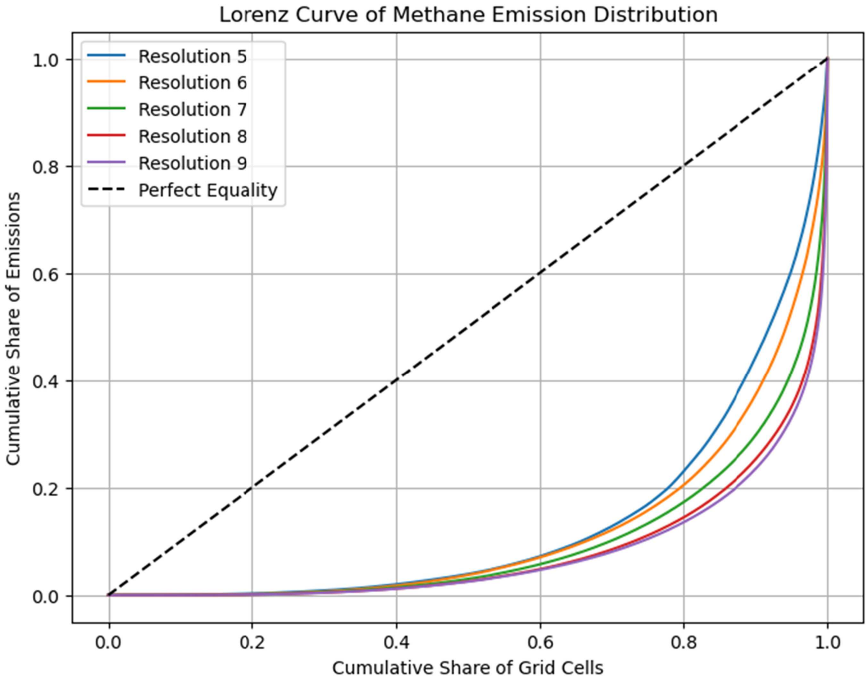

Figure 9. Lorenz curve of methane emission distribution across grid cells at rHEALPix resolutions 5 to 9.

Table 4. Spatial correlation coefficients (r) between Scarpelli's 2018 methane emission map (converted to rHEALPix DGGS) and this study's Petrinex-based methane emissions for 2020–2023, evaluated across different rHEALPix resolution levels.

	Petrinex conventional volumetric data			
Resolution level	2020	2021	2022	2023
5	0.58	0.55	0.57	0.53
6	0.32	0.31	0.30	0.28
7	0.10	0.10	0.10	<0.1
8	<0.1	<0.1	<0.1	<0.1
9	<0.1	<0.1	<0.1	<0.1

evaluate the spatial consistency between this study's methane emissions derived from Petrinex data and the existing gridded oil and gas sector inventory by Scarpelli, Jacob, Moran, et al. (2022) in Alberta, we computed the spatial correlation coefficient (r) between the two datasets. Since the Petrinex data used in this study include only intended emissions from oil and gas operations in Alberta, fugitive emissions were excluded from the work by Scarpelli, Jacob, Moran, et al. (2022) to ensure a consistent basis for comparison. We only focused on the intended emissions from upstream oil and gas operations. The comparison was performed grid-to-grid by converting Scarpelli et al. 2018 methane emissions map to the rHEALPix DGGS framework and assessing the correlation across different spatial resolutions (Table 4). Scarpelli et al. 2018 gridded inventory was initially reported on a $0.1\,^{\circ} \times 0.1\,^{\circ}$ grid, which closely corresponds to rHEALPix DGGS resolution 6, where the ellipsoidal cell area is approximately 160 km² (Table 1).

The results show that at coarser resolutions, e.g. levels 5 and 6, the correlation remains moderate, with r values ranging from 0.58 in 2020 to 0.53 in 2023 at level 5 and declining to 0.32 in 2020 and 0.28 in 2023 at level 6. However, the correlation drops substantially at the finer resolution of level 7 and above, reaching values below 0.1 at levels 8 and 9 for all years. Given that resolution 6 aligns most closely with Scarpelli et al. original grid, the moderate correlation suggests that methodological differences in emission allocation, such as facility-level spatial proxies or activity data, manifest more distinctly at localised scales. While Scarpelli, Jacob, Moran, et al. (2022) allocated emissions using proxies such as population density and GHGRP facility data, our approach directly aggregates facility-level Petrinex reports, thereby avoiding proxy-induced misallocations. The declining correlation at finer resolutions mirrors findings by Maasakkers et al. (2016), who observed similar trends when comparing EDGAR v4.2 to spatially resolved inventories. Such misallocations can propagate errors in atmospheric inversions. For instance, gridded inventories that misattribute emissions to populated areas may skew inverse model outputs, as satellite retrievals struggle to distinguish urban and industrial sources (Maasakkers et al. 2023).

Figure 10 shows the spatial comparison of Alberta's upstream intended methane emissions between Scarpelli, Jacob, Moran, et al. (2022) gridded inventory in year 2018 and this study's Petrinex-based inventory, converted to the rHEALPix DGGS framework. The difference maps shown in Figure 11 reveal that the magnitude of differences decreases at finer resolutions. This is because finer grids reduce aggregation errors, isolating discrepancies to smaller spatial units where emission values are inherently lower, even as spatial mismatches in source placement persist. For example, a hotspot misallocated by one grid cell in a coarse resolution may span multiple cells at finer resolutions, lowering per-cell differences but weakening overall correlation.

5. Discussion

5.1 Key findings and interpretation

Our DGGS-based analysis shows a highly uneven spatial distribution of upstream methane emissions in Alberta. At rHEALPix level five, the top 5% of cells account for roughly one-third of the annual total, and concentration increases at finer resolutions. These patterns align with the "super-emitter" phenomenon observed in other oil-producing regions, where a minority of sites account for a disproportionate share of sector-wide emissions (Cusworth et al. 2022 ; Lauvaux and Giron 2022). Hotspots persist across 2020 to 2023, which suggests that major emission centres are linked to stable infrastructure and operating practices rather than short-lived events. The cross-framework comparison with a graticule-based inventory that we converted to rHEALPix shows broad agreement in high-emission regions at coarse scales. It reveals divergence at finer scales, where proxy-based allocation and reporting differences have greater influence. These findings indicate that equal area and hierarchy-aware gridding separates methodological effects from projection artifacts and improves interpretability for monitoring and policy analysis. These results confirm the value of assigning facility-reported emissions at their native locations before aggregation. The hierarchy then preserves mass as totals are rolled up, which supports fair comparison across resolutions.

5.2 Practical implications and adoption guidance

The rHEALPix DGGS provides immediate practical value for methane monitoring and reporting in Alberta and in similar production regions. Equal area cells create a stable spatial unit that does not change with latitude. This enables direct comparison of emission intensity across space and through time without area normalisation, and it improves fairness in benchmarking and clarity in trend detection. The workflow begins with facility-linked assignment to rHEALPix cells, so spatial accuracy is grounded in reported locations rather than proxy redistribution. Exact aggregation across the hierarchy ensures totals are consistent at every level, improving auditability for reporting and analysis.

Each cell has a persistent identifier, which turns the grid into a standard data bucket for facilities and assets. Facility reports, infrastructure registers, maintenance records, satellite columns from TROPOMI, GHGSat, and MethaneSAT, aircraft fluxes, and tower measurements can be stored and reconciled at the exact locations regardless of their original resolution or format. The hierarchy supports consistent aggregation at any scale. Results can be aggregated in a mass-conserving way from neighbourhoods around facilities to basins and provinces and then to national summaries. Analysts can switch between multiple granularities by selecting the rHEALPix level that matches the spatial question, with coarser levels supporting regional assessment and finer levels supporting local screening. Because cell identities do not change over time, the exact locations can be used for precise hotspot tracking and for evaluating intervention outcomes. The fixed lattice also supports informed monitoring and survey design since aerial routes, revisit schedules, and ground campaigns can be planned and evaluated against the same set of cells.

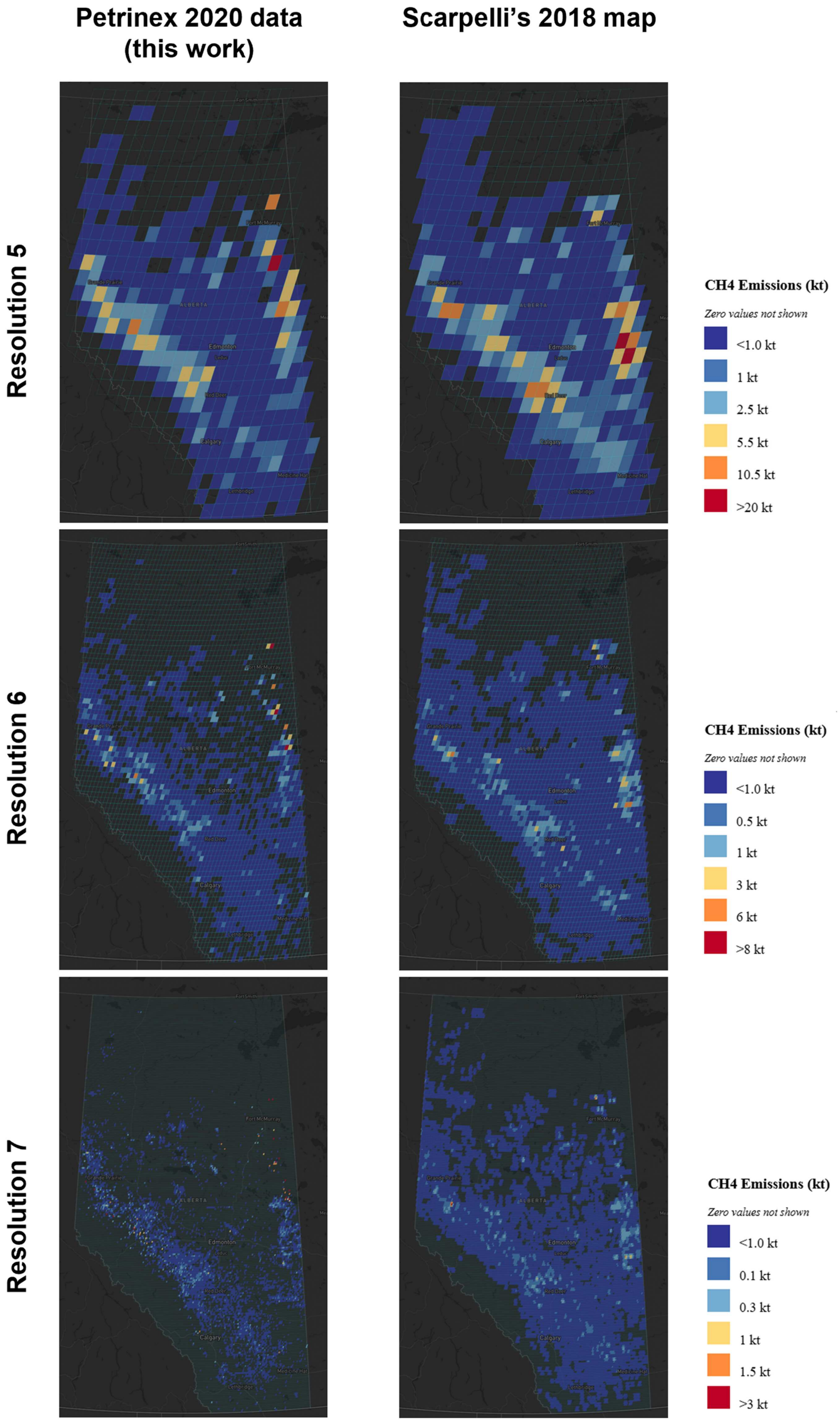

Figure 10. Alberta CH_4 emissions mapped in rHEALPix at resolutions 5 to 7. The left panel represents Petrinex 2020 data (this work), and the right panel represents Scarpelli, Jacob, Moran, et al. (2022) inventory data in year 2018 after conversion to rHEALPix.

Adoption can begin without changes to transport models or enterprise data systems. Inventory producers and modelling groups can publish priors and posteriors on native model grids and also on one or more common rHEALPix levels. Mass-conserving and area-weighted operators can translate fields between DGGS and native grids, and publishing these operators with uncertainty documentation enables transparent reuse. DGGS can serve as the standardised analysis layer for visualisation,

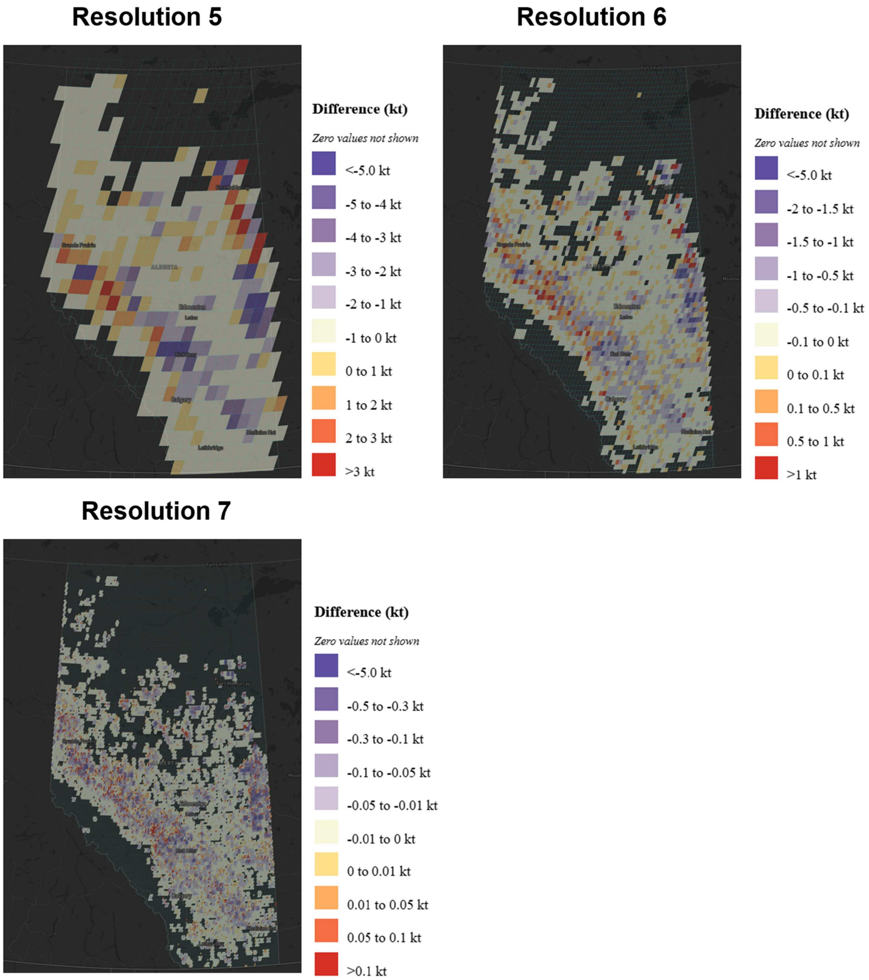

Figure 11. Inventory differences between this work in 2020 and Scarpelli, Jacob, Moran, et al. (2022) data in 2018 at rHEALPix resolutions 5 to 7. Positive values indicate higher emissions in this study.

quality control, inventory reconciliation, and regulatory reporting, while model cores and data lakes remain unchanged. In inverse modelling, a DGGS-based inventory can be directly used as the emission state, and the hierarchy allows multi-scale regularisation across parent and child cells. DGGS, therefore, can serve as a standard spatial substrate that preserves mass and spatial consistency for priors, posteriors, and operational metrics.

Equal area cells preserve spatial integrity in maps, so viewers are not misled by latitude-driven cell deformation. Each cell represents a precisely defined area, enabling quantitative reporting of emissions per unit area and improving compliance workflows. It also provides a clear definition of spatial resolution so that analysts can refer to specific cell sizes rather than terms such as urban, basin, or regional scale.

5.3 Limitations and future work

This study focuses on intended upstream emissions reported through the Petrinex portal. It does not yet include midstream or downstream sources or diffuse linear and areal components such as pipelines and urban leaks. Future work will broaden sectoral coverage and integrate satellite and aircraft constraints directly in DGGS for joint inversions. The framework can also be extended to other greenhouse gases while preserving mass at all aggregation levels. Another direction is the development of DGGS-native regularisation and uncertainty quantification that uses the hierarchy to control spatial structure across multiple scales. The framework is global and therefore well suited to Arctic monitoring, where equal-area cells avoid high-latitude distortion and support consistent tracking of permafrost-related methane signals in remote regions.

6. Conclusions

This shows that rHEALPix DGGS is a practical foundation for a spatially explicit methane inventory in Alberta's upstream oil and gas sector. By using facility-level Petrinex data within an equal-area, hierarchical grid framework, we identified persistent high-emission hotspots, revealing that 5% of grid cells account for over 34% of total annual emissions. Concentration strengthens at finer resolutions, which is consistent with super-emitter behaviour reported in other basins. The equal-area lattice removes latitude-driven bias and supports fair comparisons of intensities across space and time. Mass-conserving aggregation keeps totals consistent across resolutions, improving transparency for analysis and reporting.

Our cross-framework comparison confirms that broad patterns are shared with a graticule-based inventory at coarse scales. At the same time, differences emerge at finer scales where proxy allocation and reporting choices matter most. These findings explain why an equal area and hierarchy-aware approach improves interpretability. In practical terms, the fixed cell identifiers serve as standard data buckets for facilities and assets, enabling multi-source integration that includes satellite columns, aircraft fluxes, and ground sensors. The same cells can carry priors, posteriors, and operational metrics, and can be used to target surveys, track interventions, and support compliance.

The approach generalises beyond Alberta. It can be extended to midstream and downstream sources, as well as to other greenhouse gases, while preserving mass at every level. It also provides a natural substrate for joint use of bottom-up inventories and top-down observations. In this sense, DGGS advances the vision of a Digital Earth for methane monitoring, where emissions are referenced on a standard, equal-area lattice that is stable over time and interoperable across systems. These results support wider adoption of rHEALPix DGGS as a standard spatial substrate for methane analysis and policy workflows. It offers a clear path to consistent hotspot screening, fair intensity benchmarking, and scalable reporting from facilities to provinces and nations. With continued integration of satellite and aircraft data and broader sectoral coverage, DGGS can help deliver actionable, auditable methane insights to decision-makers.

Acknowledgements

The authors thank the staff at SensorUp Inc., Calgary, for their technical expertise and insights into processing methane emissions data from Petrinex. We are also grateful to the members of the GeoSensor Web Lab at the University of Calgary for their valuable feedback and collaborative discussions during the development of this study.

Author contributions

Conceptualisation: Mingke Li and Steve H.L. Liang; Methodology: Mingke Li and Steve H.L. Liang; Formal analysis and investigation: Mingke Li; Writing — original draft preparation: Mingke Li; Writing — review and editing: Steve H.L. Liang; Funding acquisition: Steve H.L. Liang; Supervision: Steve H.L. Liang. All authors have given final approval of the version to be published and agree to be accountable for all aspects of the work.

Disclosure statement

The authors report there are no competing interests to declare.

Funding

This research was funded by the Rogers Internet of Things Research Chair.

Data availability statement

The data that support the findings of this study are openly available in Petrinex at https://www.petrinex.ca/PD/Pages/APD.aspx.

References

Alberta Energy Regulator. 2025. *Directive 007 Volumetric and Infrastructure Requirements*. Accessed January 10. https://www.aer.ca/regulations-and-compliance-enforcement/rules-and-regulations/directives/directive-007

Alexe, M., P. Bergamaschi, A. Segers, R. Detmers, A. Butz, O. Hasekamp, S. Guerlet, et al. 2015. "Inverse Modelling of Ch4 Emissions for 2010–2011 Using Different Satellite Retrieval Products from Gosat and Sciamachy." *Atmospheric Chemistry and Physics* 15(1): 113–133. https://doi.org/10.5194/acp-15-113-2015.

Bell, J., J. Yu, B. Leighton, J. Wang, and A. Ip. 2020. *AusPix - an Australian Government implimentation of the rHealpix DGGS*. Accessed November 11 2024. https://github.com/GeoscienceAustralia/AusPIX_DGGS.

Bowater, D., and E. Stefanakis. 2019a. "On the Isolatitude Property of the rHEALPix Discrete Global Grid System." *Big Earth Data* 3(4): 362–377. https://doi.org/10.1080/20964471.2019.1658494.

Bowater, D., and E. Stefanakis. 2019b. "An Open-Source Web Service for Creating Quadrilateral Grids Based on the rHEALPix Discrete Global Grid System." *International Journal of Digital Earth* 13(9): 1055–1071. https://doi.org/10.1080/17538947.2019.1645893.

Bowater, D., and M. Wachowicz. 2020. "Modelling Offset Regions around Static and Mobile Locations on a Discrete Global Grid System: An Iot Case Study." *ISPRS International Journal of Geo-Information* 9(5): 335. https://doi.org/10.3390/ijgi9050335.

Canada Energy Regulator. 2023. Canada's Energy Future 2023: Energy Supply and Demand Projections to 2050. Accessed February 14, 2025. https://www.cer-rec.gc.ca/en/data-analysis/canada-energy-future/2023/

Crippa, M., D. Guizzardi, F. Pagani, M. Banja, et al. 2023. *GHG Emissions of All World Countries*. Luxembourg: European Commission.https://doi.org/10.2760/953322

Crippa, M., D. Guizzardi, F. Pagani, M. Schiavina, M. Melchiorri, E. Pisoni, F. Graziosi, et al. 2024. "Insights into the Spatial Distribution of Global, National, and Subnational Greenhouse Gas Emissions in the Emissions Database for Global Atmospheric Research (Edgar V8.0)." *Earth System Science Data* 16(6): 2811–2830. https://doi.org/10.5194/essd-16-2811-2024.

Cusworth, D. H., A. K. Thorpe, A. K. Ayasse, D. Stepp, J. Heckler, G. P. Asner, and C. E. Miller, et al. 2022. "Strong Methane Point Sources Contribute a Disproportionate Fraction of Total Emissions across Multiple Basins in the United States." *Proceedings of the National Academy of Sciences of the United States of America* 119(38): e2202338119. https://doi.org/10.1073/pnas.2202338119.

Gibb, R. 2016. The Rhealpix Discrete Global Grid System In *IOP Conference Series: Earth and Environmental Science, 9th Symposium of the International Society for Digital Earth (ISDE)*. Halifax, Canada: IOP Publishing Ltd. https://doi.org/10.1088/1755-1315/34/1/012012

Gibb, R., B. Cochrane, and M. Purss. 2021. "OGC Testbed-16: DGGS and DGGS API Engineering Report." Accessed November 11, 2024." http://www.opengis.net/doc/PER/t16-D017.

Gilić, F., and M. Gašparović. 2025. "Enhancing Authalic Latitude Calculation for the rHEALPix DGGS." *IEEE Journal of Selected Topics in Applied Earth Observations and Remote Sensing* 18: 12675–12683. https://doi.org/10.1109/JSTARS.2025.3567839.

Goodchild, M. F. 2018. "Reimagining the History of GIS." *Annals of GIS* 24(1): 1–8. https://doi.org/10.1080/19475683.2018.1424737.

Gorski, K. M., E. Hivon, A. J. Banday, B. D. Wandelt, F. K. Hansen, M. Reinecke, and M. Bartelmann. 2005. "HEALPix — a Framework for High Resolution Discretization, and Fast Analysis of Data Distributed on the Sphere." *The Astrophysical Journal* 622(2): 759–779. https://doi.org/10.1086/427976.

Government of Alberta. 2023. *Alberta Greenhouse Gas Quantification Methodologies Version 2.3.*Accessed October 15, 2024 https://open.alberta.ca/publications/alberta-greenhouse-gas-quantification-methodologies

Hiller, R. V., D. Bretscher, T. DelSontro, T. Diem, W. Eugster, R. Henneberger, S. Hobi, et al. 2014. "Anthropogenic and Natural Methane Fluxes in Switzerland Synthesized within a Spatially Explicit Inventory." Biogeosciences 11(7): 1941–1959. https://doi.org/10.5194/bg-11-1941-2014.

Höglund-Isaksson, L., A. Gómez-Sanabria, Z. Klimont, P. Rafaj, and W. Schöpp. 2020. "Technical Potentials and Costs for Reducing Global Anthropogenic Methane Emissions in the 2050 Timeframe –Results from the Gains Model." *Environmental Research Communications* 2(2): 025004. https://doi.org/10.1088/2515-7620/ab7457.

Hojati, M., C. Robertson, S. Roberts, and C. Chaudhuri. 2022. "GIScience Research Challenges for Realizing Discrete Global Grid Systems as a Digital Earth." *Big Earth Data* 6(3): 358–379. https://doi.org/10.1080/20964471.2021.2012912.

Huang, L., S. Stokes, Q. Chen, F. J. Cardoso-Saldaña, and D. T. Allen. 2024. "High Spatial and Temporal Resolution Simulations of Methane Column Loadings Due to Routine Emissions and Emission Events in Oil and Gas Regions." *ACS ES&T Air* 1(7): 670–677. https://doi.org/10.1021/acsestair.4c00021.

Ishizawa, M., D. Chan, D. Worthy, E. Chan, F. Vogel, J. R. Melton, and V. K. Arora. 2024. "Estimation of Canada's Methane Emissions: Inverse Modelling Analysis Using the Environment and Climate Change Canada (Eccc) Measurement Network." *Atmospheric Chemistry and Physics* 24(17): 10013–10038. https://doi.org/10.5194/acp-24-10013-2024.

Jeong, S., D. Millstein, and M. L. Fischer. 2014. "Spatially Explicit Methane Emissions from Petroleum Production and the Natural Gas System in California." *Environmental Science Technology* 48(10): 5982–5990. https://doi.org/10.1021/es4046692.

Kmoch, A., I. Vasilyev, H. Virro, and E. Uuemaa. 2022. “Area and Shape Distortions in Open-Source Discrete Global Grid Systems.” *Big Earth Data* 6(3): 256–275. https://doi.org/10.1080/20964471.2022.2094926.

Kuenen, J., S. Dellaert, A. Visschedijk, J.-P. Jalkanen, I. Super, and H. Denier van der Gon. 2022. “Cams-Reg-V4: A State-of-the-Art High-Resolution European Emission Inventory for Air Quality Modelling.” *Earth System Science Data* 14(2): 491–515. https://doi.org/10.5194/essd-14-491-2022.

Lauvaux, T., C. Giron, M. Mazzolini, A. d'Aspremont, A. d’Aspremont, R. Duren, D. Cusworth, D. Shindell, and P. Ciais. 2022. “Global Assessment of Oil and Gas Methane Ultra-Emitters.” *Science* 375(6580): 557–561. https://doi.org/10.1126/science.abj4351.

Li, M., and E. Stefanakis. 2020. “Geospatial Operations of Discrete Global Grid Systems—a Comparison with Traditional GIS.” *Journal of Geovisualization and Spatial Analysis* 4: 26. https://doi.org/10.1007/s41651-020-00066-3.

Li, M., C. Tousignant, C. Chaudhuri, and A. Chabbouh. 2024. “Utilizing Serverless Framework for Dynamic Visualization and Operations in Geospatial Applications.” *International Journal of Digital Earth* 17(1): 2392835. https://doi.org/10.1080/17538947.2024.2392835.

Loman, M. L., L. T. Murray, E. M. Leibensperger, and J. D. Maasakkers. 2025. “A High-Resolution Inventory of Anthropogenic Methane Emissions in New York State.” *Environmental Science Technology* 59(32): 16933–16946. https://doi.org/10.1021/acs.est.5c07245.

Lu, X., D. J. Jacob, H. Wang, J. D. Maasakkers, Y. Zhang, T. R. Scarpelli, L. Shen, et al. 2022. “Methane Emissions in the United States, Canada, and Mexico: Evaluation of National Methane Emission Inventories and 2010–2017 Sectoral Trends by Inverse Analysis of in Situ (Globalviewplus Ch4 Obspack) and Satellite (Gosat) Atmospheric Observations.” *Atmospheric Chemistry and Physics* 22(1): 395–418. https://doi.org/10.5194/acp-22-395-2022.

Lyon, D. R., D. Zavala-Araiza, R. A. Alvarez, R. Harriss, V. Palacios, X. Lan, and R. Talbot, et al. 2015. “Constructing a Spatially Resolved Methane Emission Inventory for the Barnett Shale Region.” *Environmental Science Technology* 49(13): 8147–8157. https://doi.org/10.1021/es506359c.

Maasakkers, J. D., D. J. Jacob, M. P. Sulprizio, A. J. Turner, M. Weitz, T. Wirth, and C. Hight, et al. 2016. “Gridded National Inventory of U.S. Methane Emissions.” *Environmental Science Technology* 50(23): 13123–13133. https://doi.org/10.1021/acs.est.6b02878.

Maasakkers, J. D., E. E. McDuffie, M. P. Sulprizio, C. Chen, M. Schultz, L. Brunelle, and R. Thrush, et al. 2023. “A Gridded Inventory of Annual 2012-2018 U.S. Anthropogenic Methane Emissions.” *Environmental Science Technology* 57(43): 16276–16288. https://doi.org/10.1021/acs.est.3c05138.

Mapbox n.d. *Mapbox: Maps and Location for Developers*. Accessed September 2, 2024. https://www.mapbox.com/.

Masson-Delmotte, V., P. Zhai, A. Pirani, and S. L. Connors, et al. 2023. *Climate Change 2021: The Physical Science Basis. Contribution of Working Group I to the Sixth Assessment Report of the Intergovernmental Panel on Climate Change*. Cambridge, United Kingdom: Intergovernmental Panel on Climate Change. https://doi.org/10.1017/9781009157896.

Miller, S. M., S. C. Wofsy, A. M. Michalak, E. A. Kort, A. E. Andrews, S. C. Biraud, and E. J. Dlugokencky, et al. 2013. “Anthropogenic Emissions of Methane in the United States.” *Proceedings of the National Academy of Sciences of the United States of America* 110(50): 20018–20022. https://doi.org/10.1073/pnas.1314392110.

Myhre, G., D. Shindell, F.-M. Bréon, and W. Collins. Anthropogenic and Natural Radiative Forcing. In *Climate Change 2013: The Physical Science Basis. Contribution of Working Group I to the Fifth Assessment Report of the Intergovernmental Panel on Climate Change* Stocker, T.F., D. Qin, G.-K. Plattner, M. Tignor, S.K. Allen, J. Doschung, A. Nauels, Y. Xia, V. Bex and P.M. Midgley, eds. 659–740, Cambridge, United Kingdom: Cambridge University Press. https://doi.org/10.1017/CBO9781107415324.018

Omara, M., R. Gautam, M. A. O'Brien, A. Himmelberger, A. Franco, K. Meisenhelder, G. Hauser, et al. 2023. “Developing a Spatially Explicit Global Oil and Gas Infrastructure Database for Characterizing Methane Emission Sources at High Resolution.” *Earth System Science Data* 15(8): 3761–3790. https://doi.org/10.5194/essd-15-3761-2023.

Omara, M., A. Himmelberger, K. MacKay, J. P. Williams, J. Benmergui, M. Sargent, S. C. Wofsy, and R. Gautam. 2024. “Constructing a measurement-based spatially explicit inventory of US oil and gas methane emissions (2021).” *Earth System Science Data* 16(9): 3973–3991. https://doi.org/10.5194/essd-16-3973-2024.

Peng, S., S. Piao, P. Bousquet, P. Ciais, B. Li, X. Lin, S. Tao, Z. Wang, Y. Zhang, and F. Zhou. 2016. “Inventory of Anthropogenic Methane Emissions in Mainland China from 1980 to 2010.” *Atmospheric Chemistry and Physics* 16(22): 14545–14562. https://doi.org/10.5194/acp-16-14545-2016.

Raichev, A., R. Gibb, and N. J. Car. 2020. *Rhealpixdggs*. Accessed August 5, 2024. https://github.com/manaakiwhenua/Rhealpixdggs-py.

Scarpelli, T. R., D. J. Jacob, M. Moran, F. Reuland, and D. Gordon. 2022. “A Gridded Inventory of Canada’s Anthropogenic Methane Emissions.” *Environmental Research Letters* 17(1): 014007. https://doi.org/10.1088/1748-9326/ac40b1.

Scarpelli, T. R., E. Roy, D. J. Jacob, M. P. Sulprizio, R. D. Tate, and D. H. Cusworth. 2025. “Using New Geospatial Data and 2020 Fossil Fuel Methane Emissions for the Global Fuel Exploitation Inventory (Gfei) V3.” *Earth System Science Data*. preprint. https://doi.org/10.5194/essd-2024-552.

Scarpelli, T. R., D. J. Jacob, C. A. Octaviano Villasana, I. F. Ramírez Hernández, P. R. Cárdenas Moreno, E. A. Cortés Alfaro, M. &A. García García, and D. Zavala-Araiza. 2020. “A Gridded Inventory of Anthropogenic Methane

Emissions from Mexico Based on Mexico's National Inventory of Greenhouse Gases and Compounds." *Environmental Research Letters* 15(10): 105015. https://doi.org/10.1088/1748-9326/abb42b.

Scarpelli, T. R., D. J. Jacob, J. D. Maasakkers, M. P. Sulprizio, J. Sheng, K. Rose, L. Romeo, J. R. Worden, and G. Janssens-Maenhout. 2020. "A Global Gridded (0.1° × 0.1°) Inventory of Methane Emissions from Oil, Gas, and Coal Exploitation Based on National Reports to the United Nations Framework Convention on Climate Change." *Earth System Science Data* 12(1): 563–575. https://doi.org/10.5194/essd-12-563-2020.

Scarpelli, T. R., D. J. Jacob, S. Grossman, X. Lu, Z. Qu, M. P. Sulprizio, Y. Zhang, F. Reuland, D. Gordon, and J. R. Worden. 2022. "Updated Global Fuel Exploitation Inventory (GFEI) for Methane Emissions from the Oil, Gas, and Coal Sectors: Evaluation with Inversions of Atmospheric Methane Observations." *Atmospheric Chemistry and Physics* 22(5): 3235–3249. https://doi.org/10.5194/acp-22-3235-2022.

Sheng, J., S. Song, Y. Zhang, R. G. Prinn, and G. Janssens-Maenhout. 2019. "Bottom-up Estimates of Coal Mine Methane Emissions in China: A Gridded Inventory, Emission Factors, and Trends." *Environmental Science & Technology Letters* 6(8): 473–478. https://doi.org/10.1021/acs.estlett.9b00294.

Turner, A. J., D. J. Jacob, K. J. Wecht, J. D. Maasakkers, E. Lundgren, A. E. Andrews, S. C. Biraud, et al. 2015. "Estimating Global and North American Methane Emissions with High Spatial Resolution Using Gosat Satellite Data." *Atmospheric Chemistry and Physics* 15(12): 7049–7069. https://doi.org/10.5194/acp-15-7049-2015.

Varon, D. J., D. J. Jacob, B. Hmiel, R. Gautam, D. R. Lyon, M. Omara, M. Sulprizio, et al. 2023. "Continuous Weekly Monitoring of Methane Emissions from the Permian Basin by Inversion of Tropomi Satellite Observations." *Atmospheric Chemistry and Physics* 23(13): 7503–7520. https://doi.org/10.5194/acp-23-7503-2023.

Wang, Y. P., and S. T. Bentley. 2002. "Development of a Spatially Explicit Inventory of Methane Emissions from Australia and Its Verification Using Atmospheric Concentration Data." *Atmospheric Environment* 36(1): 4965–4975. https://doi.org/10.1016/S1352-2310(02)00589-7.

Wecht, K. J., D. J. Jacob, C. Frankenberg, Z. Jiang, and D. R. Blake. 2014. "Mapping of North American Methane Emissions with High Spatial Resolution by Inversion of Sciamachy Satellite Data." *Journal of Geophysical Research: Atmospheres* 119(12): 7741–7756. https://doi.org/10.1002/2014jd021551.

Zhang, Y., R. Gautam, S. Pandey, M. Omara, J. D. Maasakkers, P. Sadavarte, D. Lyon, et al. 2020. "Quantifying Methane Emissions from the Largest Oil-Producing Basin in the United States from Space." *Science advances* 6(17): eaaz5120. https://doi.org/10.1126/sciadv.aaz5120.